Ore Geology Reviews 125 (2020) 103676

Contents lists available at ScienceDirect

Ore Geology Reviews

journal homepage: www.elsevier.com/locate/oregeorev

Two episodes of REEs mineralization at the Sin Quyen IOCG deposit, NW Vietnam

Xuan Dac Ngo[a,b], Xin-Fu Zhao[a,*], Thanh Hai Tran[b], Xiao-Dong Deng[a], Jian-Wei Li[a]

[a] State Key Laboratory of Geological Processes and Mineral Resources, and School of Earth Resources, China University of Geosciences, Wuhan 430074, China
[b] Department of Mineral Resource Prospecting and Exploration, Hanoi University of Mining and Geology, Hanoi, Viet Nam

ARTICLE INFO

Keywords:
Sin Quyen deposit
Allanite, titanite
In situ isotopic analysis
Multiple episodes of mineralization

ABSTRACT

The Sin Quyen iron oxide-copper–gold (IOCG) deposit in northwestern Vietnam contains a proven reserve of 52.8 Mt ores at 14% Fe, 0.91% Cu, 0.7% REEs (rare earth elements), and 0.44 g/t Au. REEs mineralization is hosted within Ca-silicate alteration zone and associated with Fe-Cu ore bodies in the gneiss, mica schist, and marble of the Upper Sin Quyen Formation. Two mineralization episodes are identified based on the field and petrographic relations. The first episode includes sodic alteration (stage I-1), calcic alteration and associated REE mineralization (stage I-2), and localized K-Fe alteration (stage I-3). The second episode is main stage mineralization and contains four main stages of alteration: pre-ore Na alteration (stage II-1), Ca-Fe alteration and the associated Fe-REE mineralization (stage II-2), K-Fe alteration and associated Cu-Au mineralization (stage II-3), and the final carbonate stage of quartz-carbonate veins (stage II-4) crosscutting the above-mentioned alteration phases and ores.

Primary allanite and type 1 titanite (Tnt-1) from episode 1 yield weighted mean $^{206}Pb/^{238}U$ ages of 882 ± 3 Ma and 881 ± 8 Ma (2σ), respectively, which are interpreted as the timing of REE mineralization in episode 1. Secondary allanite and type 2 titanite (Tnt-2) associated with iron-oxide and Cu-Au ores, however, have U-Pb ages of 840 ± 7 Ma and 838 ± 5 Ma (2σ), respectively. These ages are hence considered to represent the timing of polymetallic IOCG mineralization in episode 2. ~880 Ma titanite grains have $\varepsilon_{Nd}(t)$ values ranging from −7.00 to −5.43, which are intermediate between the Neoproterozoic felsic intrusions and ore-hosting *meta*-sedimentary rocks in the region and likely reflect interaction between magmatic fluids and ore-hosting rocks. In contrast, ~840 Ma titanite have $\varepsilon_{Nd}(t)$ values ranging from −4.31 to −1.97, similar to those of the Neoproterozoic felsic intrusions, indicating a possible magmatic fluid source for the episode II IOCG mineralization. Multiple episodes of mineralization at Sin Quyen were likely formed during the prolonged tectonothermal events related to backarc extension during the Neoproterozoic subduction along the western margin of the Yangtze Block.

1. Introduction

Iron oxide-copper–gold (IOCG) deposits are characterized by pervasive alkali (Na-Ca-K) alteration and generally associated with magmatic-hydrothermal systems under an extensional tectonic setting (Hitzman et al., 1992; Groves et al., 2010). Previous studies have shown that many IOCG deposits may have formed by multiple hydrothermal events or underwent post-ore hydrothermal overprint in a prolonged tectonothermal history (e.g. Barton (2014); Zhao et al. (2017); Zhu et al. (2017)). As such, precise constraints on the timing and history of IOCG deposits is of critical importance in better understanding their genesis, evolution, and geodynamic setting.

Sin Quyen is the largest IOCG deposit in Vietnam, and may represent the southern extension of the Kangdian IOCG belt along the western Yangtze Block in SW China (Zhao and Zhou, 2011). This deposit was discovered in 1975, but precise dating of ore mineralization had not been performed until the most recent effort. Ishihara et al. (2011) speculated that the REE-Fe-Cu mineralization at Sin Quyen was likely related to the Cenozoic alkaline granitic magmatism in the region but without any isotopic dating. Li et al. (2017) firstly reported U-Pb dating of hydrothermal zircon and monazite at ~840 Ma for the Fe-REE mineralization at Sin Quyen. Our recent field and petrographic investigations suggest that the Sin Quyen deposit may have undergone multiple magmatic-hydrothermal events, necessitating further geochronological study to comprehensively understand the mineralization history of the deposit.

* Corresponding author.
E-mail address: xfzhao@cug.edu.cn (X.-F. Zhao).

https://doi.org/10.1016/j.oregeorev.2020.103676
Received 6 January 2020; Received in revised form 20 June 2020; Accepted 7 July 2020
Available online 15 July 2020

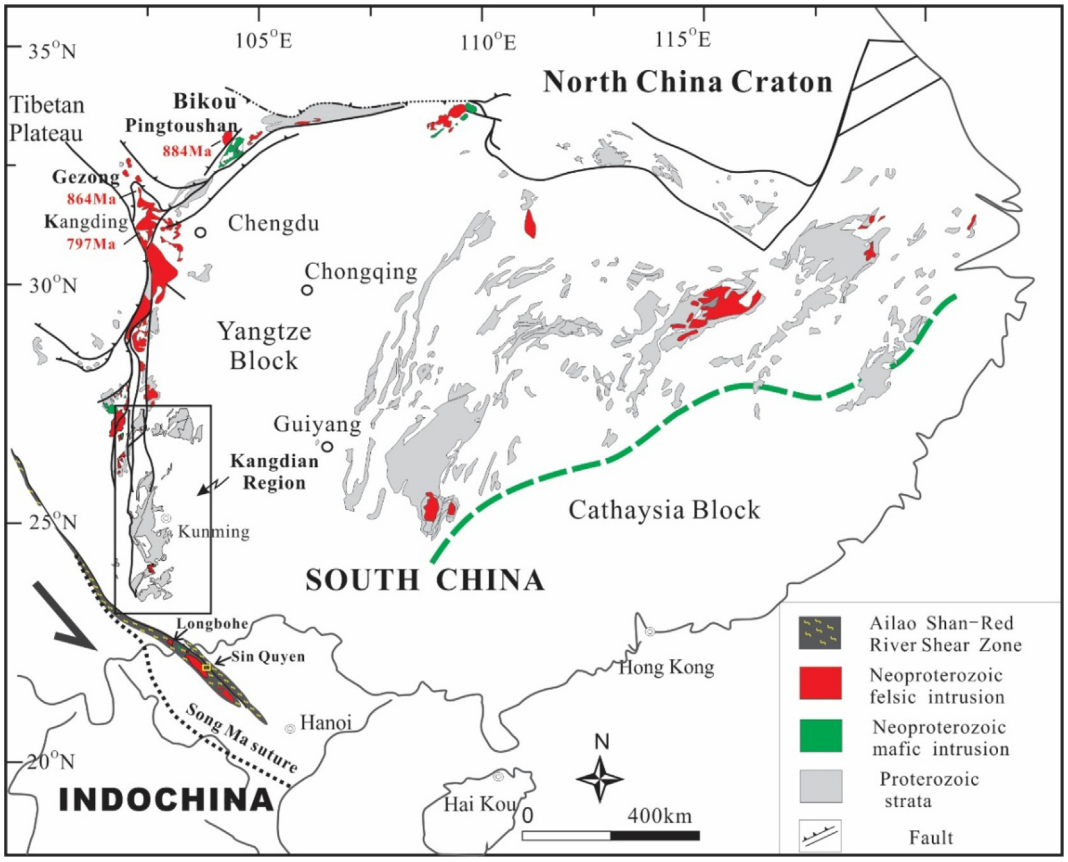

Fig. 1. Simplified regional map highlighting the distribution of Neoproterozoic igneous rocks in South China and Northwest Vietnam (after Zhao and Zhou (2011)). The ages of the Pingtoushan diorite are from Xiao et al. (2007), and Kangding gneiss and Gezong granite are from Zhou et al. (2002).

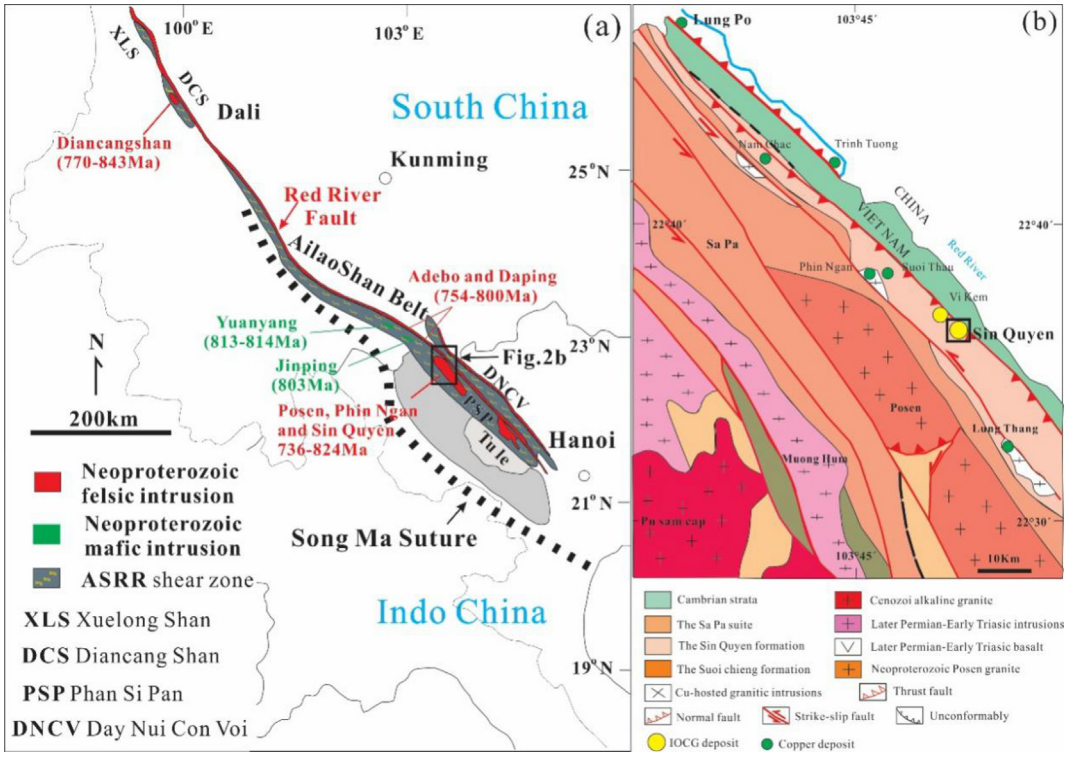

Fig. 2. (a) Simplified geotectonic map of northwestern Vietnam and southwestern China, showing the location of major tectonic units and highlighting the distribution of Neoproterozoic igneous rocks. The ages of the Diancangshan felsic intrusions are from Liu et al. (2015); the Yuanyang and Jinping mafic intrusions from Cai et al. (2014); the Adebo and Daping felsic intrusions from Qi et al. (2012) and Cai et al., (2015); the Posen and Phin Ngan felsic intrusions from Wang et al. (2011) and Li et al. (2017a). (b) Geological map of the Sin Quyen-Lung Po belt, showing the distribution of Fe-Cu-Au deposits (after Tran et al. (2014)).

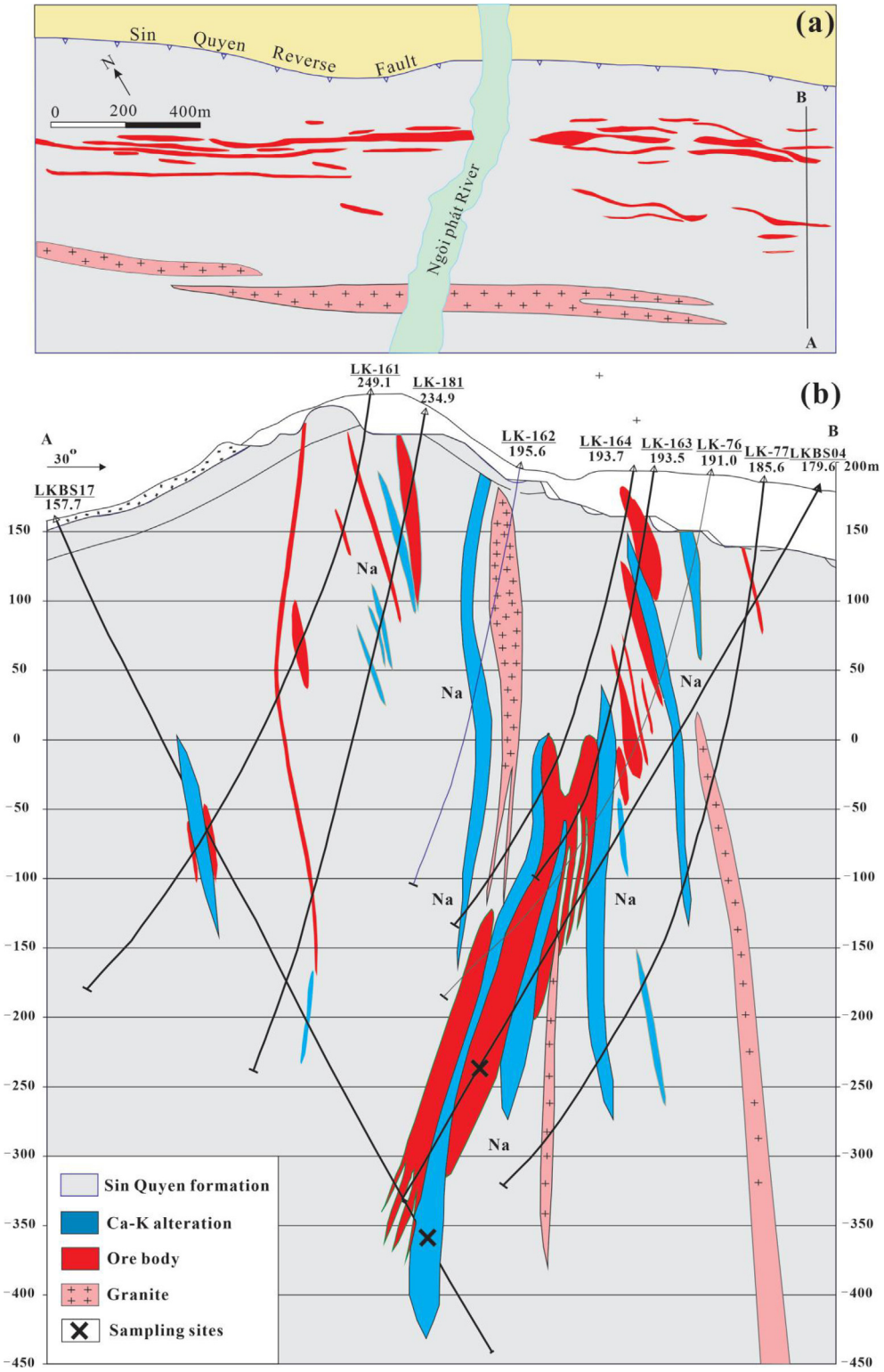

Fig. 3. Simplified geological map of the Sin Quyen deposit (modified from Ta, 1975).

In this paper, we present new U-Pb ages and Sm-Nd isotopes of allanite and titanite, which provide new insights into the formation and evolution of the Sin Quyen deposit. We firstly use paragenetic and textural data to characterize two generations of hydrothermal allanite and titanite, which are associated with REE-only and Fe-REE-Cu-Au mineralization, respectively. We then carry out in-situ U-Pb isotope analyses of allanite and titanite to precisely constrain the timing of the two ore formation events. Laser ablation (MC)-ICP-MS trace elements and Nd isotopic analyses were also conducted to provide additional evidence supporting that the REE-only and Fe-REE-Cu-Au mineralization were formed from contrasting hydrothermal fluids. Finally, a possible relation between the Sin Quyen deposit and the IOCG metallogenic belt along western Yangtze Block is also evaluated based on recently-published data.

Fig. 4. (a) A large lenticular orebody hosted in mica-schist in the Sin Quyen deposit. (b) The massive ore bodies are crosscut by a granitic dike. (c) Early stage-amphibole-allanite zone are overprinted by magnetite and chalcopyrite. (d) Banded magnetite and chalcopyrite ores. (e) A typical massive allanite ore sample in the first mineralization event. (f) A typical massive Fe-Cu ore sample in the second mineralization event.

2. Regional geology

The Sin Quyen deposit is located in the southwestern portion of the Ailao Shan-Red River (ASRR) shear zone in northwestern Vietnam (Fig. 1). Large areas of northwestern Vietnam have been affected by two major tectonothermal events since the early Mesozoic. The first is the amalgamation of the South China Block and the Indochina Block along the Song Ma suture zone at ~250 Ma (Chung et al., 1998; Liu et al., 2015). The second is the sinistral strike-slip movement along the ASRR shear zone due to the Cenozoic India-Eurasia collision (Tapponnier

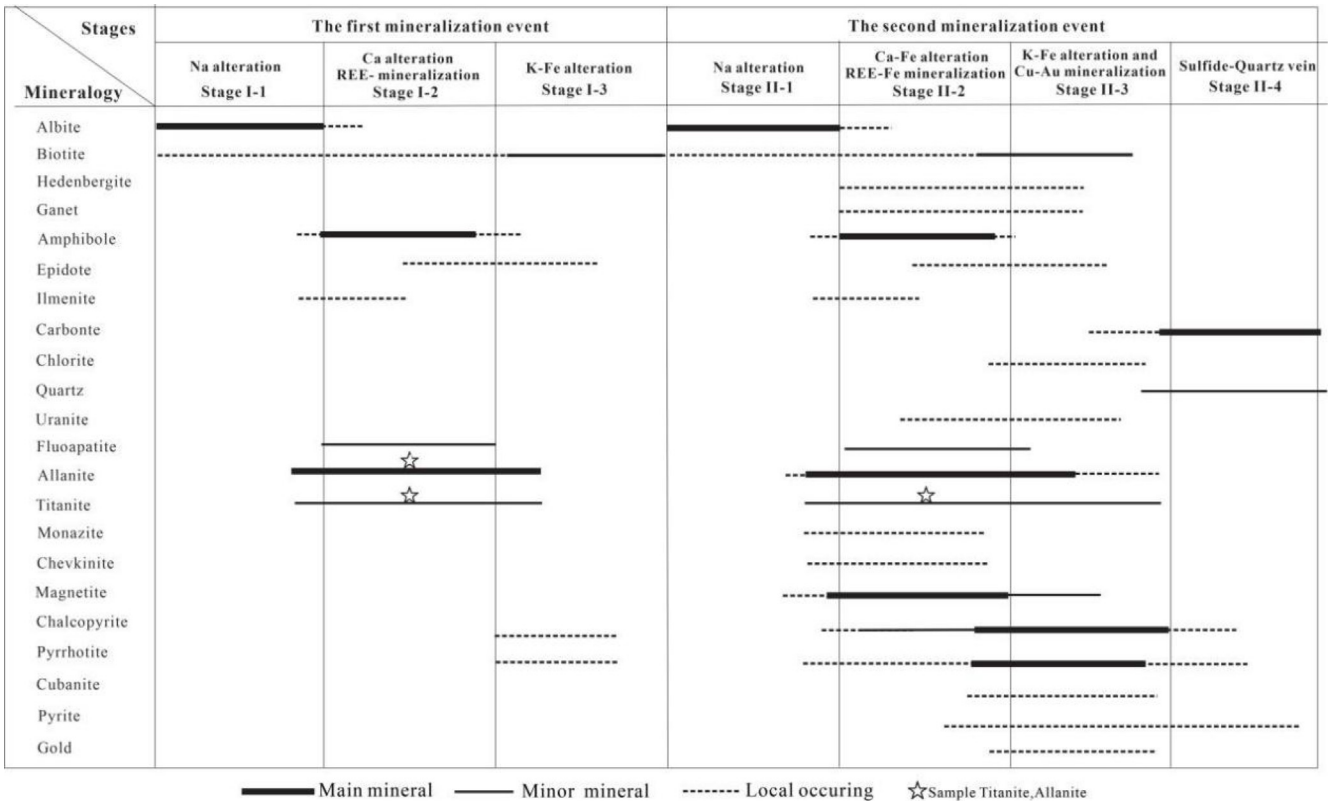

Fig. 5. Paragenetic sequence of mineralization and alteration in the Sin Quyen deposit. REE-minerals include allanite, titanite, monazite, xenotime; Carbonate minerals include calcite (compiled from Li et al. (2017b, 2018) and this study).

et al., 1990; Leloup et al., 1995). Structural movement along the ASRR Fault has led to southeastward displacement of the Indochina peninsula relative to South China by a distance of ~500 km (Fig. 1). It is therefore believed that northwestern Vietnam is tectonically affiliated to the western Yangtze Block (Chung et al., 1998; Hieu et al., 2011; Li et al., 2017a). The ASRR shear zone consists of four narrow metamorphic belts, including, from northwest to southeast, Xuelong Shan, Diancang Shan, Ailao Shan-Phan Si Pan, and Day Nui Con Voi (Fig. 2a; Leloup et al., 1995; Liu et al., 2015).

The Phan Si Pan belt in NW Vietnam is dominated by a high-grade metamorphic complex consisting of the Suoi Chieng and Sin Quyen formations and is unconformably covered by Paleozoic-Early Triassic sedimentary rocks (Fig. 2b). The protoliths of the metamorphic complex include Archean to Paleoproterozoic granitoids (Lan et al., 2001) and Paleoproterozoic to Neoproterozoic sedimentary and mafic volcanic rocks. The Suoi Chieng Formation is mainly composed of granitic gneiss, biotite schist, biotite-amphibole gneiss, and amphibolite. The Sin Quyen Formation is underlain by the Suoi Chieng Formation and consists of mica schist, gneiss, and minor marble. Detrital zircons of the Sin Quyen Formation have U-Pb ages that cluster at 2.5–2.3 Ga, 1.9–1.7 Ga, 1.6–1.3 Ga, and 1.0–0.88 Ga (Hieu et al., 2010, 2011; Wang et al., 2011; Liu and Chen, 2019).

Granitoid intrusions are widespread in the Phan Si Pan belt (Fig. 2b), and have emplacement ages of Neoproterozoic, late Permian to early Triassic, and Cenozoic (Wang et al., 2011; Hieu et al., 2013; Usuki et al., 2015; Liu et al., 2015; Tran et al., 2016). The Neoproterozoic granitoid intrusions mainly include the Posen, Phin Ngan, and Lung Thang plutons together with several small stocks (Fig. 2b; Li et al., 2017a). They have arc-like geochemical signatures, such as enrichment of LILE (e.g., Rb, Th, and U) and LREE and depletion of HFSE (e.g., Nb, Ti, and P), which have been interpreted as products of subduction-related magmatism (Li et al., 2017a). The Neoproterozoic intrusions in the Ailao Shan-Phan Si Pan belt are well comparable to the equivalents (~860 to ~740 Ma) widely distributed in the western Yangtze Block (Fig. 1; Zhou et al., 2002; Zhao et al., 2008; Cai et al., 2014, 2015; Li et al., 2017a). The late Permian to Early Triassic Muong Hum pluton mostly emplaced within the 259–249 Ma interval (Fig. 2b; Hieu et al., 2013; Usuki et al., 2015). The Cenozoic intrusions are largely represented by the Pu Sam Cap alkaline complex and have zircon U-Pb ages of 35–33 Ma (Fig. 2b; Tran et al., 2015; Liu et al., 2015).

3. The Sin Quyen deposit

The Sin Quyen-Lung Po district in the northeastern segment of the Ailao Shan-Phan Si Pan belt contains > 10 Fe-Cu deposits, forming the most important Cu metallogenic province in Vietnam (Fig. 2b). The largest Sin Quyen deposit has proven reserves of 52.8 Mt ores at 14% Fe, 0.91% Cu, 0.7% LREE (La, Ce, and Nd), and 0.44 g/t Au (McLean, 2001). Recent deep drillings down to 550 m depth have revealed additional resources exceeding 90 Mt of ores with an average grade of 0.9% Cu (Pham, 2015). Open-pit mining at Sin Quyen started in 2006, with an average annual production of ~30,000 t of metal Cu. Rare earth elements are present in high concentrations but have not yet been recovered.

The Sin Quyen deposit consists of 17 lenticular and sheet-like ore bodies, mostly striking east–west and dipping steeply to the north or south (Fig. 3). Individual ore bodies are 50–600 m long, 5–100 m wide, and have a maximum vertical extent of 350 m spanning from 50 to 450 m above sea level. The orebodies are hosted in the mica schists and marbles of the Sin Quyen Formation (Fig. 4a), and typically have massive (Fig. 4 c, e, f) or banded structures (Fig. 4d). In the mining area, there are several felsic dikes dominated by monzogranite, granodiorite, and granite (Figs. 3b, 4b). Zircon U-Pb dating results indicate that the dikes emplaced between 736 ± 8 Ma and 758 ± 6 Ma (Li et al., 2017a). Mafic dikes can be also observed in the mining district, but their ages are unknown. They have been variably altered to an

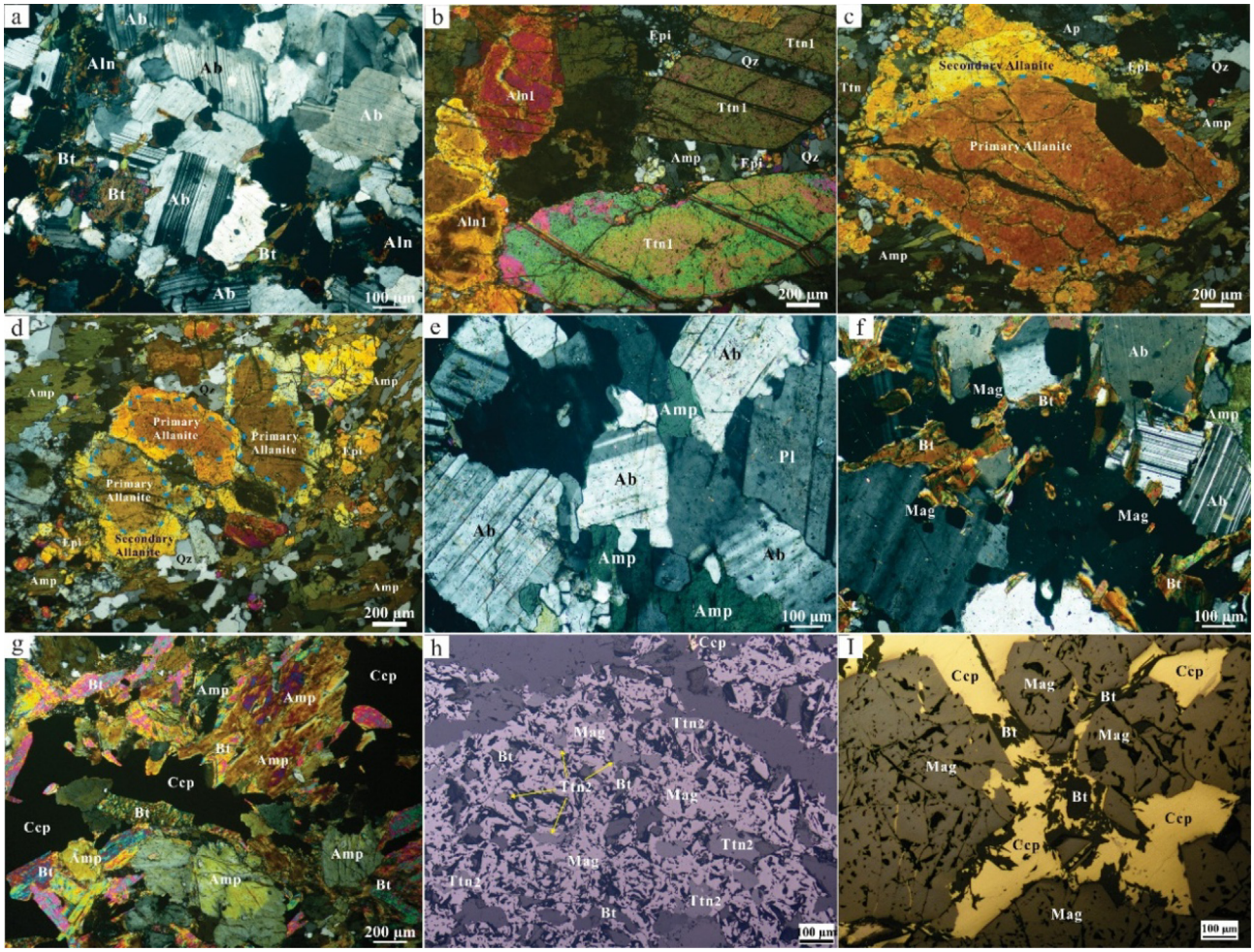

Fig. 6. Photomicrographs of representative alteration minerals of episode 1 (a–d) and 2 (e–i). (a) Early-stage albite grains overprinted by late-stage allanite and biotite of episode 1 mineralization event. (b) Big allanite and titanite (Ttn 1) grains associated with amphibole and less amount of epidote. (c-d) Allanite grain have been variably altered to form secondary allanite, which are overprinted by late-stage epidote. (e) The country rocks with extensive albitization of episode 2. (f) Early-stage albite grains overprinted by late-stage amphibole, biotite and magnetite. (g) Amphibole grains overprinted by biotite and chalcopyrite. (h) Small titanite grains (Ttn2) from the second mineralization event associated with magnetite, and biotite. (i) Biotite intergrown with chalcopyrite and magnetite. Abbreviations: Aln1-allanite from episode 1, Ttn1-titanite from episode 1, Ttn2-titanite from episode 2, Amp-amphibole, Epi-epidote, Bt-biotite; Ap-fluorapatite, Pl-plagioclase, Qz-quartz, Mag-magnetite, Ccp-chalcopyrite.

assemblage of chlorite, actinolite, epidote, sericite, and magnetite of greenschist/amphibolite facies. Previous studies have identified three main stages of alteration and mineralization at Sin Quyen deposit: (I) pre-ore Na alteration; (II) Ca-(K) alteration and associated Fe-REE mineralization; and (III) Cu-Au mineralization (Li et al., 2017b, 2018). Our field and petrographic observations, however, suggest two episodes of alteration and mineralization exist in the Sin Quyen deposit (Fig. 5). Episode 1 is characterized by REE-only ores associated with Ca-skarn minerals. It consists of pre-ore Na alteration in the ore-hosting metasedimentary rocks (stages I-1) (Fig. 6a), which was overprinted by localized but intensive Ca alteration and associated REE mineralization (stage I-2). The REE-only mineralization samples are characterized by abundant amphibole, allanite, and titanite with lesser amounts of biotite and epidote (Fig. 6b). Under the microscope, some amphibole grains show irregular zonation, implying later-stage fluid-assisted metasomatism. Allanite typically occurs as large (200–1000 μm), euhedral to subhedral crystals that are locally replaced by epidote (stage I-3) (Fig. 6c, d). The Episode 2 mineralization and alteration is expressed by a paragenetic sequence generally comparable to that described in Li et al. (2017). This includes four stages of alteration: pre-ore Na alteration (stage II-1), Ca-K alteration and associated Fe-LREE mineralization (stage II-2), K-Fe alteration and associated Cu-Au mineralization (stage II-3), and post-ore younger quartz-sulfide veins (II-4). The pre-ore sodic alteration is widely distributed in the mining area and typically present as albite replacing the ore hosting rocks (Fig. 6e). Minor amounts of euhedral magnetite occur as either interstitial to or are enclosed by albite (Fig. 6f). The extensive sodic alteration was followed by localized and intensive Ca-Fe and K-Fe alteration. The Ca-Fe alteration consists of amphibole, titanite, magnetite, and chalcopyrite (Fig. 6g, h), whereas K-Fe alteration is dominated by biotite that is commonly intergrown with chalcopyrite (Fig. 6i).

4. Samples and analytical methods

4.1. Samples

Two borehole samples, which represent the REE-only mineralization of episode 1 (Sample SQ428) and REE-Fe-Cu-Au mineralization of episode 2 (sample SQ300), respectively, were conducted for in situ elemental and isotopic analyses in this study. Sample SQ428 consists of allanite (35 vol%), amphibole (30 vol%), titanite (20 vol%), apatite (7 vol%), epidote (5 vol%), and biotite (2 vol%) with traces of chalcopyrite. This sample was prepared as polished thin section for in situ analysis of trace elements, U-Pb and Nd isotopes for allanite and

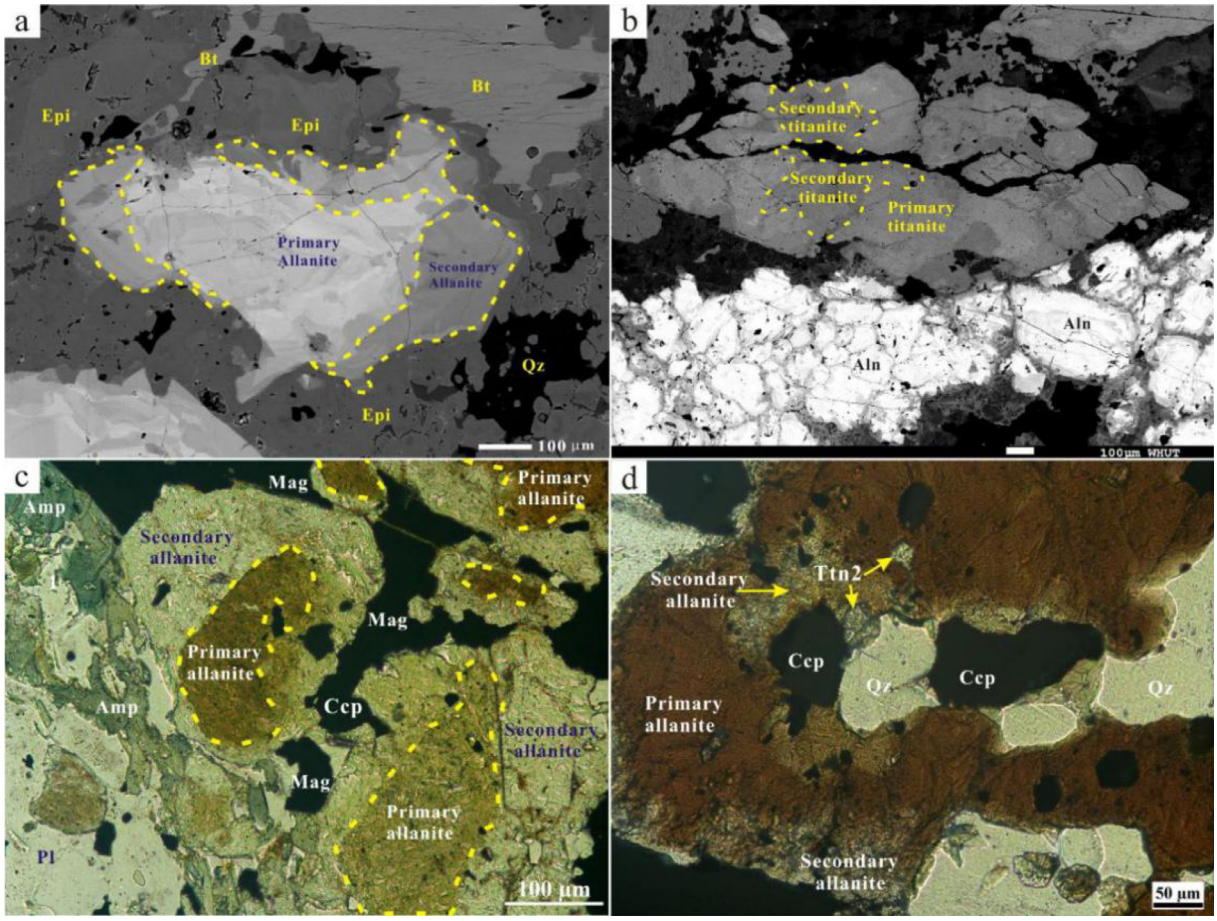

Fig. 7. BSE images (a-b) and microscopic photos (c-d) for representative allatite and titanite. (a) BSE-images of allanite reveal core-rim textures, indicating that secondary allanite was formed by partial replacement of primary allanite. (b) BSE-images reveal titanite with complex zonation: primary titanite was variably replaced by secondary titanite. (c) and (d) Allanite grains have metasomatized rims with associated magnetite, chalcopyrite, and Ttn2, indicating that secondary allanite and Ttn 2 were coevally formed. Abbreviations: Aln-allanite, Ttn2-titanite from episode 2, Amp-amphibole, Epi-epidote, Bt-biotite, Qz-quartz, Mag-magnetite, Ccp-chalcopyrite.

Table 1
Representative electronic microprobe compositions (wt%) of primary and secondary allanite in the Sin Quyen deposit.

Element	Primary allanite (n = 28)		Secondary allanite (n = 18)	
	Range	Mean	Range	Mean
SiO_2	33.32–35.17	34.20	33.32–35.17	34.20
TiO_2	0.20–0.44	0.31	0.20–0.44	0.31
Al_2O_3	16.29–17.90	16.93	16.29–17.90	16.93
FeO	13.49–15.94	15.04	13.49–15.94	15.04
MnO	0.02–0.11	0.06	0.02–0.11	0.06
MgO	0.04–0.17	0.11	0.04–0.17	0.11
CaO	16.15–17.90	16.88	16.15–17.90	16.88
La_2O_3	4.20–5.73	4.84	4.20–5.73	4.84
Ce_2O_3	5.82–7.87	6.84	5.82–7.87	6.84
Pr_2O_3	0.21–0.62	0.48	0.21–0.62	0.48
Nd_2O_3	1.10–1.66	1.39	1.10–1.66	1.39
ThO_2	0.00–0.13	0.03	0.00–0.13	0.03
P_2O_5	0.00–0.05	0.02	0.00–0.05	0.02
F	0.00–0.48	0.19	0.00–0.48	0.19
Cl	0.00–0.04	0.01	0.00–0.04	0.01
Total	94.61–98.45	97.24	92.53–97.75	96.67

titanite. Sample SQ300 consists of magnetite (40 vol%), chalcopyrite (15 vol%), biotite (15 vol%), allanite (5 vol%), epidote (5 vol%), plagioclase (3 vol%), titanite (3 vol%), and amphibole (3 vol%), with minor amounts of quartz and pyrrhotite. Titanite grains from this sample were separated using conventional heavy liquid and magnetic methods, and then handpicked under a binocular microscope. The representative titanite grains were mounted in an epoxy resin and then polished to expose their interiors, which are used for trace elements, U-Pb and Nd isotopes analyses.

4.2. Analytical methods

4.2.1. SEM and EMPA analysis

In order to identify REE minerals and their associated mineral assemblages in the specimens, the polished thin sections were detailed examined using both SEM and EPMA techniques, focusing on morphology and texture of REE minerals.

The polished thin sections were firstly examines using a FEI Quanta200 environmental scanning electron microscope (SEM), which is fitted with an energy dispersive spectrometry (EDS) system, at China University of Geosciences. Back-scattered electron (BSE) images were used to further characterize the internal textures of allanite and titanite, before in situ analyses were made.

Major elements of allanite and titanite were analyzed using a JAX 8230 electron microprobe (EMP) at the Center for Material Research and Analysis, Wuhan University of Technology. The operating conditions were established at an acceleration voltage of 25 kV, a probe current of 50nA, and a beam diameter of 5 µm for allanite, and were 15 kV, 20nA and 1 µm for titanite. The counting time for all of the elements were 20 s. EMP analysis of REEs was conducted using X-ray mapping with negligible interference as described in Scherrer et al.

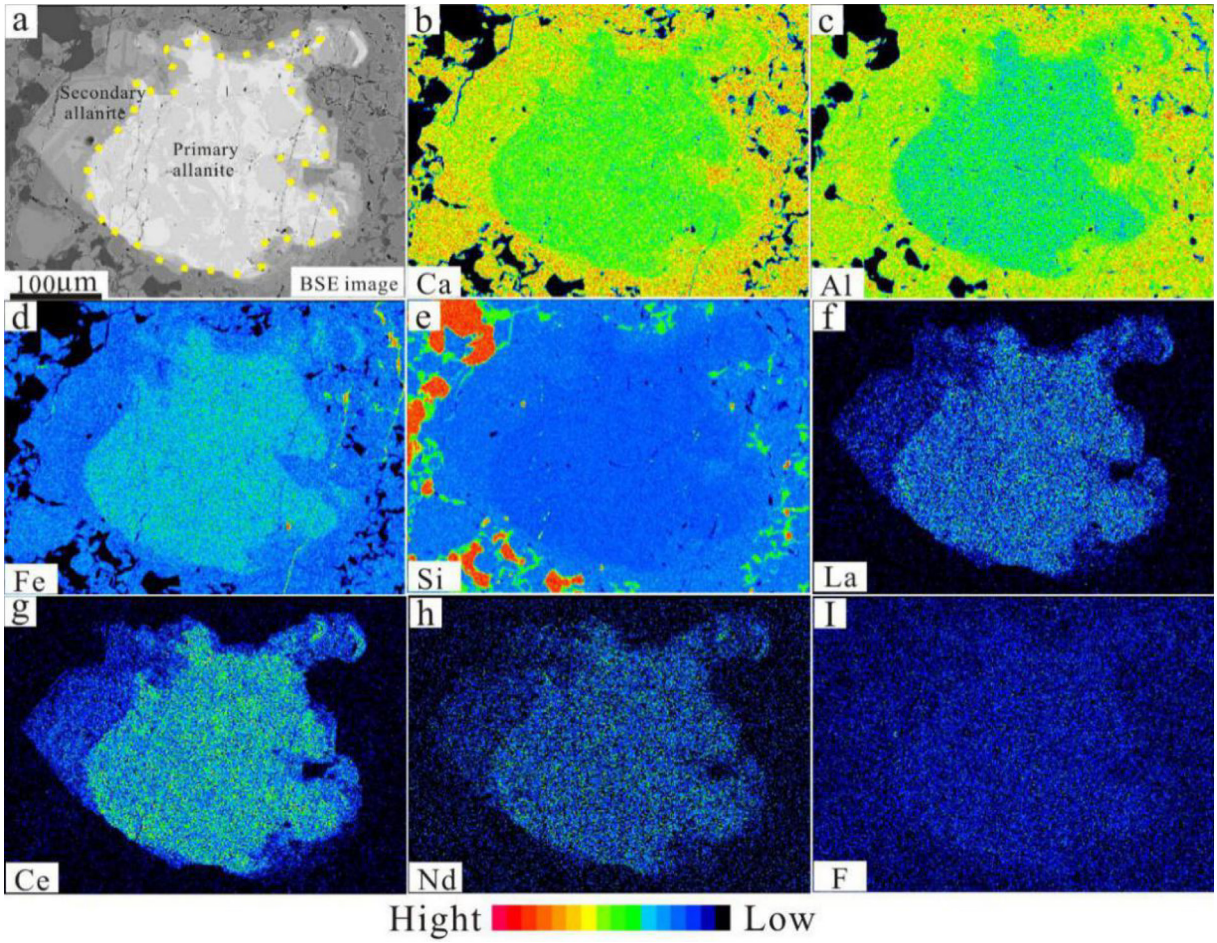

Fig. 8. (a) BSE-image and (b-i) EPMA X-ray mapping of an allanite grain with metasomatized texture, note that the increase of Ca, Al, and Si and decrease of Fe, La, Ce, Nd, and F concentrations from core to rim.

(2000). An allanite grain was selected for EPM-WDS mapping to define the spatial distribution of Ca, Al, Fe, Si, La, Ce, Nd, and F. The mapping was conducted at an accelerating voltage of 20 kV and a beam current of 30nA, with a point dwell time of 10 ms. The standards include $NaAlSi_3O_8$ (Na, Si and Al), TiO_2 (Ti), Fe_2O_3 (Fe), $CaSi_2O_6$ (Ca), $Na_8Al_2Be_2Si_8O_{24}$(Cl, S)$_2$ (Cl), CaF_2 (F), and synthetic REE phosphate.

4.2.2. LA-ICPMS trace element and U-Pb isotope analysis

Trace elements and U-Pb isotopes of allanite and titanite were simultaneously analyzed using an Agilent 7700x ICP-MS apparatus equipped with a GeoLas 2005 laser-ablation system with a DUV 193 nm ArF-excimer laser (MicroLas, Germany) at China University of Geosciences. A "wire" signal smoothing device is included in this laser ablation system, which can produce smooth signals even at very low laser repetition rates down to 1 Hz (Hu et al., 2008, 2015). The fluencies, ablation rates, and spot sizes for allanite analyses were set to 6 J/cm^2, 5 Hz, and 32 μm, while those for titanite analyses were conducted at 6 J/cm^2, 10 Hz, and 60 μm, respectively. Argon was used as the make-up gas and mixed with helium as the carrier gas via a T-connector before entering the ICP. Nitrogen was added into the central gas flow (Ar^+ He) of the Ar plasma to decrease the detection limit and improve precision, consequently increasing the sensitivity for most elements by a factor of 2 to 3 (Hu et al., 2008). Each analysis incorporated a background acquisition of 20–30 s (gas blank) followed by 50 s data acquisition.

In this study, zircon standard 91,500 was used as a calibration standard for mass discrimination and $^{207}Pb/^{206}Pb$ isotope fractionation for allanite analysis, while allanite from the Mina Monchi Fe-U-REE deposit, Burguillos Del Cerro, SW Spain (338 ± 1.5 Ma; Casquet et al., 2001) was used as an external standard for correcting U/Pb isotope fractionation. Trace elements were calibrated against the glass standard NIST SRM610, combined with internal standardization (Si). For titanite analysis, MKED1 (1517 ± 0.32 Ma; Spandler et al., 2016) was used as an external standard for mass discrimination and U-Pb isotope fractionation. Trace elements were calibrated against the glass standard NIST SRM610, combined with internal standardization (Ca). Off-line selection and integration of background and analyzed signals, and time-drift correction and quantitative calibration for trace element analyses and U-Pb dating were performed using the in-house software ICPMS-DataCal (Liu et al., 2010). Concordia diagrams and weighted mean calculations were made using Isoplot/Ex_ver3 (Ludwig, 2003). Concordia diagrams and $^{206}Pb/^{238}U$ weighted mean calculations of allanite and titanite were made using Isoplot/Ex_ver3 (Ludwig, 2003).

4.2.3. LA-MC-ICP-MS Nd isotope analysis

In situ Nd isotope analysis of titanite was performed on a Neptune Plus MC-ICP-MS (Thermo Fisher Scientific, Bremen, Germany) equipped with a Geolas HD excimer ArF laser ablation system (Coherent, Göttingen, Germany) at the Wuhan Sample Solution Analytical Technology. In the laser ablation system, helium was used as the carrier gas within the ablation cell and was merged with argon (makeup gas) after the ablation cell. Small amounts of nitrogen were added to the argon makeup gas flow for the improvement of sensitivity of Nd isotopes (Xu et al., 2015). The spot diameter of 90 μm was adopted dependent on Nd signal intensity. The pulse frequency was 10 Hz and laser fluence was kept constant at ~8 J/cm^2. A new signal-

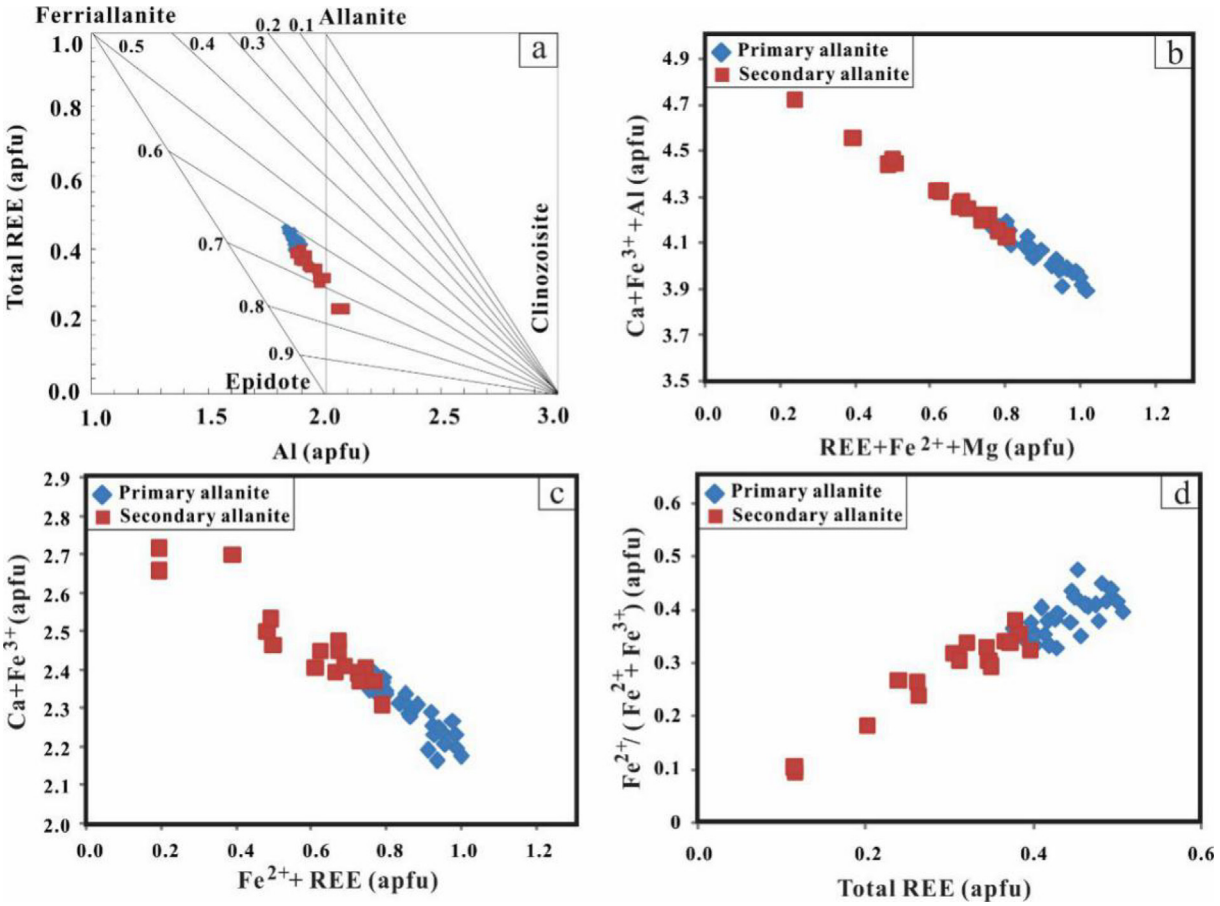

Fig. 9. (a) Plot of total REE (apfu) versus Al (apfu). (b) Plot of total Ca + Al + Fe^{3+} (apfu) versus total REE + Fe^{2+} + Mg (apfu). (c) Plot of total Fe^{2+} + REE (apfu) versus total Ca^{+} + Fe^{3+} (apfu). (d) Plot of $Fe^{2+}/(Fe^{3+} + Fe^{2+})$ versus total REE (apfu). The allanite data were obtained by EPMA.

Table 2
LA-ICP-MS trace element data (ppm) of the primary and secondary allanite in the Sin Quyen deposit.

Element	Primary allanite (n = 36)		Secondary allanite (n = 13)	
	Range	Mean	Range	Mean
P	24–153	97.19	24–122	80.92
Ti	1081–1814	1447	750–1718	1269
Sr	147–275	181	106–184	145
Y	36–1771	599	108–1216	530
Nb	0.00–0.12	0.05	0.01–0.10	0.03
La	28341–41944	37,071	18982–42649	31,900
Ce	41262–61092	53,668	27674–62565	45,992
Pr	3051–4644	4023	2161–4602	3458
Nd	8203–12190	10,794	5731–12434	9300
Sm	589–965	799	444–982	707
Eu	140–558	375	245–479	351
Gd	138–507	334	197–468	299
Tb	6.50–64	30.79	14.50–50.7	28.11
Dy	14.10–376	142	41–268	129
Ho	1.30–60.10	20.41	4–41.20	18.10
Er	2.70–141.7	47.04	6.60–104	40.97
Tm	0.20–14.60	5.12	0.50–13.0	4.47
Yb	1.70–88	32.95	2.90–89.9	28.15
Lu	0.20–7.00	2.88	0.20–7.60	2.35
Hf	0.00–1.25	0.74	0.52–1.80	0.96
Ce/La	1.40–1.50	1.45	1.41–1.50	1.44

Table 3
Representative electronic microprobe compositions (wt%) of type 1 titanite and type 2 titanite in the Sin Quyen deposit.

Element	Type 1 titanite (n = 18)		Type 2 titanite (n = 18)	
	Range	Mean	Range	Mean
SiO_2	30.17–31.14	30.75	29.22–30.94	30.34
TiO_2	31.53–36.87	34.46	34.63–40.18	36.50
Al_2O_3	2.26–4.17	2.95	1.15–2.60	1.60
Na_2O	0.00–0.03	0.01	0.00–0.04	0.02
K_2O	0.00–0.00	0.00	0.00–0.01	0.002
FeO	1.13–2.24	1.96	0.57–1.78	1.42
MnO	0.00–0.07	0.03	0.02–0.10	0.06
CaO	27.95–29.70	29.09	28.53–30.12	29.13
F	0.83–1.70	1.16	0.24–0.98	0.52
Cl	0.00–0.04	0.00	0.00–0.02	0.00

smoothing device was used downstream from the sample cell to efficiently eliminate the short-term variation of the signal and remove the mercury from the background and sample aerosol particles (Hu et al. 2015). The mass discrimination factor for $^{143}Nd/^{144}Nd$ was determined using $^{146}Nd/^{144}Nd$ (0.7219) with the exponential law. The ^{149}Sm signal was used to correct the remaining ^{144}Sm interference on ^{144}Nd, using the $^{144}Sm/^{149}Sm$ ratio of 0.2301. Two natural titanite megacrysts, MKED1 and SP-Ttn-01, were used as the unknown samples to verify the accuracy of the calibration method for in situ Nd isotope analysis of titanite.

5. Results

5.1. Textures and compositions of allanite and titanite

5.1.1. Allanite

Allanite is abundant in the episode 1 REE-only mineralization at Sin

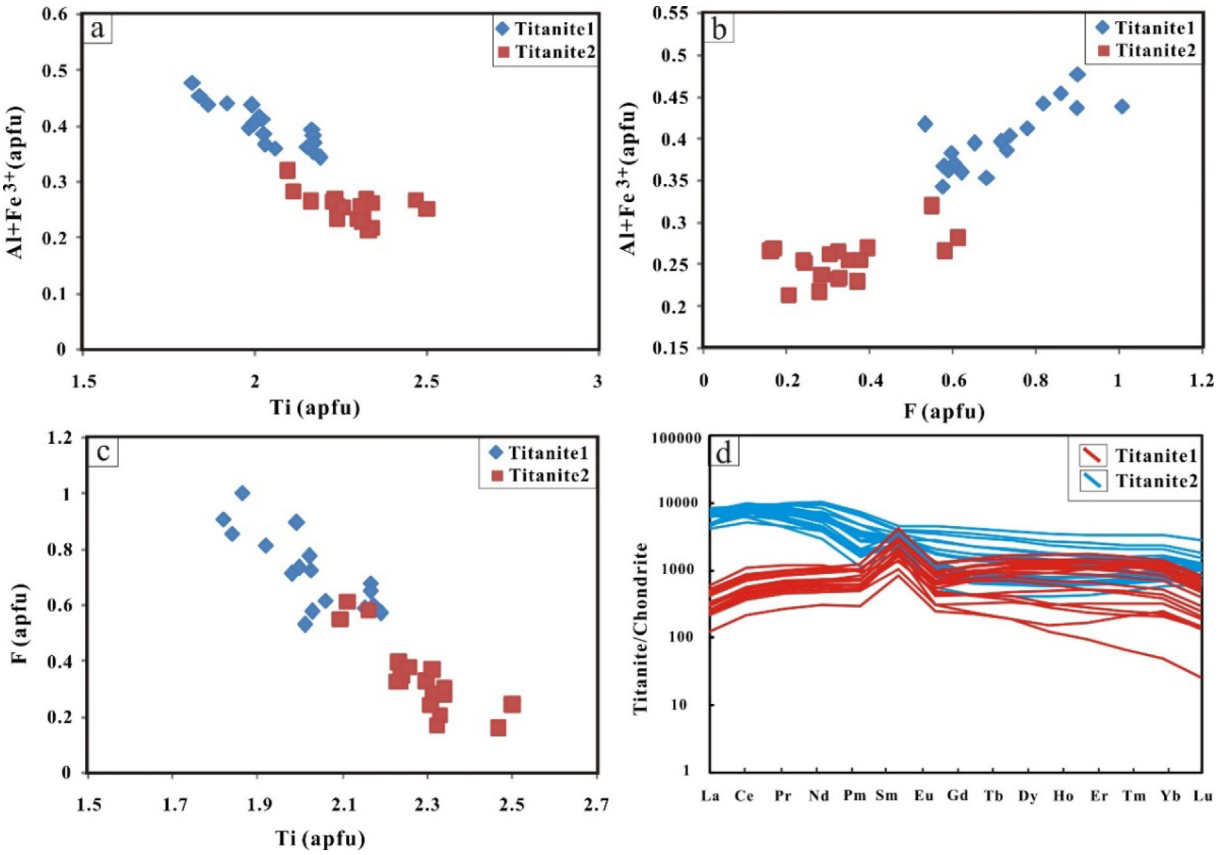

Fig. 10. (a) The negative relationship between Al + Fe^{3+} (apfu) and Ti (apfu) of titanite. (b) The negative relationship between Al + Fe^{3+} (apfu) and F (apfu) of titanite. (c) The negative relationship between F (apfu) and Ti (apfu) of titanite. (d) Chondrite-normalized REE pattern of type 1 titanite and type 2 titanite. The titanite data were obtained by EPMA.

Table 4
LA-ICP-MS trace element data (ppm) of type 1 titanite and type 2 titanite in the Sin Quyen deposit.

Element	Type 1 titanite (n = 20)		Type 2 titanite (n = 17)	
	Range	Mean	Range	Mean
Y	235–3840	1759	707–5161	2099
La	36–176	101	986–1972	1443
Ce	164–810	451	3242–6250	4831
Pr	31–140	83	412–961	694
Nd	172–694	433	1392–4986	2955
Sm	56–232	147	169–1138	542
Eu	59–305	163	109–263	174
Gd	61–326	176	117–946	404
Tb	11–69	38	16–156	62
Dy	58–522	286	104–974	387
Ho	9–130	63	23–198	77
Er	19–431	192	71–567	218
Tm	2.04–68.93	28.01	12–86	33
Yb	10–420	167	98–583	237
Lu	0.78–37.41	14.32	15–71	30
Hf	19.25–48.89	32	15–43	27
δEu	1.81–4.18	3.11	0.74–2.25	1.33
ΣREE	690–3814	2342	7758–17311	12,087
LREE/HREE	0.70–5.45	1.84	3.83–16.38	9.10
Lu/Hf	0.03–1.09	0.45	0.67–2.13	1.14

Quyen. It typically occurs as euhedral to subhedral crystals of 0.5–2 mm, and may have core-rim textures consisting of an early generation in the core and a late generation forming the rim, hereafter termed as primary and secondary allanite (Figs. 6c, 7a). The primary allanite is closely associated with titanite and amphibole (Fig. 6b), whereas the secondary allanite is variably related to magnetite and chalcopyrite (Fig. 7c). Results of EMP analysis (Table 1 and Appendix A1) show that the primary allanite grains have 4.20–5.73 wt% of La_2O_3, 5.82–7.87 wt% of Ce_2O_3, and 1.10–1.66 wt% of Nd_2O_3, which are significantly higher than those of the secondary variety (1.37–4.14 wt% of La_2O_3, 1.84–6.32 wt% of Ce_2O_3, and 0.34–1.46 wt% of Nd_2O_3). In comparison, the secondary allanite has higher CaO (16.83–22.29 wt%) than primary allanite (16.15–17.90 wt%). The contents of Pr_2O_3, MgO, MnO, TiO_2, and P_2O_5 in the two allanite generations are similar and generally lower than 1.0 wt%. The compositional variations between the primary and secondary allanite revealed by EMP analysis are confirmed by the X-ray mapping (Fig. 8), in which the primary domains are distinctly higher in LREE (e.g., La, Ce, add Nd), Fe and F, but lower in Ca, Si, and Al relative to the secondary domains (Fig. 8b–i). Both the primary and secondary allanite have high Ce/La atomic ratios (1.4–1.5) and thus are classified as allanite-(Ce) (Table A1; Fig. 9a). There is a strongly positive correlation between REE^{3+} + Fe^{2+} + Mg and Ca^{2+} + Al^{3+} + Fe^{3+}, and between REE^{3+} + Fe^{2+} and Ca^{2+} + Fe^{3+} in atoms per formula unit (apfu) (Fig. 9b, c). This correlation indicates a substitution mechanism of REE^{3+} + Fe^{2+} → Ca^{2+} + Al^{3+} in allanite (Petrik et al.1995; Giere and Sorensen 2004; Chen and Zhou, 2014). The primary allanite typically has $Fe^{2+}/(Fe^{3+}$ + $Fe^{2+})$ ratios (0.35–0.49) higher than those of secondary allanite (0.10–0.38) (Fig. 9d).

Trace element compositions determined by LA-ICPMS confirm the results of EMP analysis (Table 2 and Appendix A1). No obvious difference in MREEs and HREEs exist between the primary allanite and secondary allanite. All allanite grains have low, variable Th and U contents ranging from 47 to 387 ppm and from 145 to 547 ppm, respectively. For allanite grains with core-rim textures, the rims and cores have Th/U ratios of 0.18–0.60 and 0.15–1.07, respectively (Table 5).

Table 5
In situ LA-ICP-MS U–Th–Pb ages of primary and secondary allanite in the Sin Quyen deposit.

Spots	$_{Common}$Pb ppm	$_{Total}$Pb ppm	Th ppm	U ppm	Th/U	$^{207}Pb/^{206}Pb$		$^{207}Pb/^{235}U$		$^{206}Pb/^{238}U$	
						Ratio	2σ	Ratio	2σ	Ratio	2σ
H-01P	0.0	67.5	64	322	0.20	0.0622	0.0030	1.2740	0.0563	0.1476	0.0023
H-02P	7.7	59.8	47	316	0.15	0.0644	0.0030	1.3212	0.0570	0.1479	0.0023
H-03P	23.2	60.7	79	176	0.45	0.0673	0.0045	1.3510	0.0881	0.1445	0.0023
H-04P	0.0	71.4	80	284	0.28	0.0666	0.0033	1.3727	0.0659	0.1486	0.0022
H-05P	0.0	78.3	93	270	0.34	0.0693	0.0036	1.4100	0.0707	0.1468	0.0023
H-06P	4.4	69.8	107	162	0.66	0.0721	0.0047	1.4549	0.0890	0.1460	0.0026
H-07P	30.4	87.8	117	239	0.49	0.0722	0.0041	1.4948	0.0793	0.1496	0.0024
H-08S	30.3	59.0	69	271	0.25	0.0667	0.0036	1.2726	0.0650	0.1379	0.0023
H-09P	37.2	67.0	74	255	0.29	0.0706	0.0039	1.4418	0.0751	0.1475	0.0024
H-10P	26.3	71.9	84	246	0.34	0.0713	0.0040	1.4305	0.0727	0.1452	0.0025
H-11S	24.0	80.4	122	203	0.60	0.0697	0.0042	1.3537	0.0778	0.1403	0.0026
H-12S	27.6	74.1	78	341	0.23	0.0668	0.0034	1.3160	0.0641	0.1421	0.0022
H-13P	24.5	78.0	71	362	0.19	0.0719	0.0035	1.4427	0.0679	0.1446	0.0021
H-14S	0.0	95.8	103	421	0.24	0.0681	0.0033	1.3385	0.0594	0.1422	0.0021
H-15P	14.0	81.5	89	334	0.27	0.0678	0.0032	1.3711	0.0632	0.1463	0.0026
H-16P	0.0	56.2	82	145	0.57	0.0671	0.0043	1.3804	0.0820	0.1493	0.0029
H-17P	91	85.3	73	397	0.18	0.0714	0.0039	1.4198	0.0712	0.1441	0.0024
H-18P	0.0	62.9	65	288	0.22	0.0661	0.0034	1.3292	0.0643	0.1456	0.0022
H-19P	38.3	74.3	103	214	0.48	0.0690	0.0042	1.4130	0.0842	0.1475	0.0023
H-20P	3.9	71.6	109	200	0.55	0.0661	0.0036	1.3805	0.0727	0.1508	0.0027
H-21P	0.0	64.3	84	224	0.37	0.0652	0.0040	1.2887	0.0723	0.1432	0.0025
H-22P	59.0	77.8	88	322	0.27	0.0670	0.0035	1.3499	0.0655	0.1454	0.0023
H-23S	0.0	89.6	94	534	0.18	0.0621	0.0031	1.1415	0.0521	0.1326	0.0021
H-24P	9.8	66.5	87	220	0.40	0.0715	0.0042	1.4593	0.0789	0.1479	0.0028
H-25P	37.6	108.1	139	387	0.36	0.0668	0.0034	1.3533	0.0649	0.1464	0.0023
H-26P	27.8	83.5	108	290	0.37	0.0667	0.0039	1.3529	0.0724	0.1470	0.0022
H-27P	26.5	76.0	85	321	0.26	0.0660	0.0034	1.3448	0.0714	0.1468	0.0022
H-28P	27.0	72.4	75	346	0.22	0.0675	0.0039	1.3335	0.0742	0.1431	0.0021
H-29S	10.0	68.8	67	279	0.24	0.0646	0.0033	1.2028	0.0557	0.1344	0.0023
H-30P	5.7	125.4	161	298	0.54	0.0668	0.0031	1.3760	0.0584	0.1488	0.0025
H-31P	33.2	142.4	165	390	0.42	0.0709	0.0029	1.4455	0.0555	0.1473	0.0021
H-32P	0.0	115.2	133	317	0.42	0.0676	0.0030	1.4041	0.0602	0.1498	0.0024
H-33P	9.4	109.2	132	246	0.54	0.0730	0.0035	1.5148	0.0691	0.1498	0.0025
H-34S	0.5	83.0	86	283	0.30	0.0738	0.0038	1.3978	0.0675	0.1368	0.0022
H-35P	41.3	166.2	202	447	0.45	0.0696	0.0035	1.4131	0.0660	0.1466	0.0026
H-36P	25.1	121.6	151	298	0.51	0.0704	0.0040	1.4198	0.0735	0.1458	0.0024
H-37P	7.1	181.0	218	496	0.44	0.0665	0.0027	1.3632	0.0510	0.1483	0.0021
H-38P	4.1	182.4	219	498	0.44	0.0672	0.0026	1.3579	0.0508	0.1458	0.0020
H-39S	21.6	82.5	88	323	0.27	0.0711	0.0037	1.3655	0.0674	0.1389	0.0024
H-40P	4.1	121.2	138	357	0.39	0.0665	0.0033	1.3436	0.0631	0.1461	0.0023
H-41P	0.0	121.9	161	274	0.59	0.0643	0.0040	1.3193	0.0797	0.1484	0.0023
H-42P	0.0	130.1	169	312	0.54	0.0629	0.0032	1.2689	0.0616	0.1458	0.0022
H-43P	3.3	155.4	167	547	0.31	0.0653	0.0027	1.3069	0.0511	0.1448	0.0020
H-44P	0.0	255.8	387	362	1.07	0.0681	0.0029	1.3723	0.0573	0.1458	0.0022
H-45S	13.9	127.9	160	410	0.39	0.0660	0.0029	1.2672	0.0531	0.1390	0.0020
H-46S	31.3	110.2	124	408	0.30	0.0633	0.0030	1.2117	0.0541	0.1385	0.0023
H-47S	11.7	85.9	87	304	0.28	0.0694	0.0035	1.3286	0.0676	0.1382	0.0026
H-48S	80.6	139.8	141	409	0.35	0.0614	0.0054	1.3296	0.0581	0.1375	0.0024
H-49S	17.2	91.1	91	409	0.22	0.0667	0.0029	1.2576	0.0530	0.1361	0.0020

Note: P: primary, S: secondary.

Spots	$^{207}Pb/^{206}Pb$		$^{207}Pb/^{235}U$		$^{206}Pb/^{238}U$	
	Age (Ma)	2σ	Age (Ma)	2σ	Age (Ma)	2σ
H-01P	680	108	834	25	888	13
H-02P	767	100	827	25	889	13
H-03P	856	138	840	38	870	13
H-04P	833	104	849	28	893	12
H-05P	907	109	864	30	883	13
H-06P	991	134	883	37	879	15
H-07P	994	117	899	32	899	13
H-08S	828	107	806	29	833	13
H-09P	946	113	877	31	887	13
H-10P	966	114	873	30	874	14
H-11S	920	126	841	34	846	15
H-12S	831	138	825	28	856	12
H-13P	983	98	878	28	871	12
H-14S	872	101	835	26	857	12
H-15P	861	103	848	27	880	15
H-16P	839	133	852	35	897	16
H-17P	969	111	868	30	868	14

(*continued on next page*)

Table 5 (*continued*)

Spots	$^{207}Pb/^{206}Pb$		$^{207}Pb/^{235}U$		$^{206}Pb/^{238}U$	
	Age (Ma)	2σ	Age (Ma)	2σ	Age (Ma)	2σ
H-18P	809	114	831	28	876	13
H-19P	900	126	866	35	887	13
H-20P	809	110	852	31	905	15
H-21P	781	125	813	32	863	14
H-22P	839	109	839	28	875	13
H-23S	680	110	747	25	803	12
H-24P	972	116	885	33	889	15
H-25P	831	140	841	28	881	13
H-26P	828	121	841	31	884	12
H-27P	807	114	837	31	883	13
H-28P	854	120	832	32	862	12
H-29S	763	114	775	26	813	13
H-30P	831	90	850	25	894	14
H-31P	954	81	879	23	886	12
H-32P	857	91	862	25	900	13
H-33P	1013	92	907	28	900	14
H-34S	1037	106	859	29	827	12
H-35P	917	104	866	28	882	14
H-36P	943	117	868	31	877	14
H-37P	833	81	845	22	891	12
H-38P	856	81	843	22	878	11
H-39S	959	106	846	29	838	13
H-40P	820	103	837	27	879	13
H-41P	750	132	826	35	892	13
H-42P	706	107	804	28	877	12
H-43P	787	90	821	22	872	11
H-44P	872	85	849	25	877	12
H-45S	806	86	804	24	839	11
H-46S	720	100	779	25	836	13
H-47S	910	−94	830	30	834	14
H-48S	654	189	831	25	830	13
H-49S	829	87	800	24	822	11

Note: P: primary, S: secondary.

5.1.2. Titanite

Two types of titanite are identified in the Sin Quyen deposit. Type 1 titanite (Ttn1) occurs as euhedral to subhedral crystals that are 0.5–2 mm in diameter, and are closely associated with amphibole and allanite (Fig. 6b). BSE images reveal that some type 1 grains also have core-rim textures, with the primary titanite being replaced by the secondary varieties (Fig. 7b). Type 2 titanite (Ttn2) occurs as homogeneous, small grains closely associated with magnetite (Fig. 6h) from sample H505. It is noted that Ttn2 may be associated with the secondary allanite (Fig. 7d).

The major element compositions of titanite are summarized in Table 3 and complete dataset is available in Appendix Table A1. Primary Ttn1 has 2.26–4.17 wt% of Al_2O_3, 1.13–2.24 wt% of FeO, and 0.83–1.70 wt% of F, which are significantly higher than those of the type 2 variety (1.15–2.60 wt%, 0.57–1.78 wt%, and 0.24–0.98 wt%, respectively). In contrast, Ttn2 has higher TiO_2 (34.63–40.18 wt%) than Ttn1 (31.53–36.87 wt%). Both Ttn1 and Ttn2 are characterized by a negative correlation between Al + Fe^{3+} and Ti (Fig. 10a) and a positive correlation between Al + Fe^{3+} and F (Fig. 10b). Meanwhile, F is negatively correlated with Ti (Fig. 10c). These correlations indicate a substitution mechanism of (Al, Fe^{3+}) + (F, OH) ↔ Ti + O in titanite (Cao et al., 2015).

The trace element compositions of titanite determined by LA-ICPMS are presented in Table 4 and Appendix A1. Ttn1 grains have moderate U (63–410 ppm) and low Th (0.17–1.50 ppm) contents, with Th/U ratios less than 0.01. They have highly variable LREE concentrations (518–2098 ppm) and low LREE/HREE ratios of 0.70–5.45. In the chondrite-normalized REE patterns, Ttn1 displays positive Eu anomalies with δEu values ranging from 1.81 to 4.18 (Fig. 10d). Hafnium and Lu contents range from 19.3 to 48. 9 ppm and 0.78 to 37.4 ppm, respectively, corresponding to low Lu/Hf values of 0.03–1.09. Ttn2 contains moderate U similar to Ttn1 (262–563 ppm), but has much higher Th (43–246 ppm) with Th/U ratios of 0.09–0.70. Compared to Ttn1, Ttn2 contains significantly higher LREE (6901–13730 ppm), and LREE/HREE (3.83–16.38) and Lu/Hf (0.67–2.13) ratios. In the chondrite-normalized REE patterns, the Ttn2 either displays negative or positive Eu anomalies with δEu of 0.74–2.25.

5.2. U-Pb ages

5.2.1. Allanite

The U-Pb isotope data of allanite are summarized in Table 5 and plotted in the concordia diagram (Fig. 11a). All spot analyses yield concordant U-Pb dates that form two coherent groups on the U-Pb concordia diagram. Thirty-six LA-ICPMS spot analyses on the primary allanite have a weighted mean $^{206}Pb/^{238}U$ age of 882 ± 3 Ma (2σ, MSWD = 0.2; Fig. 11a). Thirteen LA-ICPMS spot analyses on the secondary allanite yield concordant to nearly concordant U-Pb dates ranging from 803 ± 12 to 857 ± 12 Ma with a weighted mean $^{206}Pb/^{238}U$ age of 840 ± 7 Ma (2σ, MSWD = 2.8; Fig. 11a). The two ages are hence considered to be the crystallization ages for primary and secondary allanite, respectively.

5.2.2. Titanite

Data of titanite U-Pb dating are summarized in Table 6. All spot analyses yield nearly concordant U-Pb ages that form two coherent groups on the U-Pb concordia diagram (Fig. 11b). Twelve spots analyses on Ttn1 have a weighted mean $^{206}Pb/^{238}U$ age of 881 ± 8 Ma (2σ, MSWD = 2.2), whereas eight spots on the secondary rims of Ttn1 and seventeen spots analyses on Ttn2 together yield a weighted mean $^{206}Pb/^{238}U$ age of 838 ± 5 Ma (2σ, MSWD = 1.8).

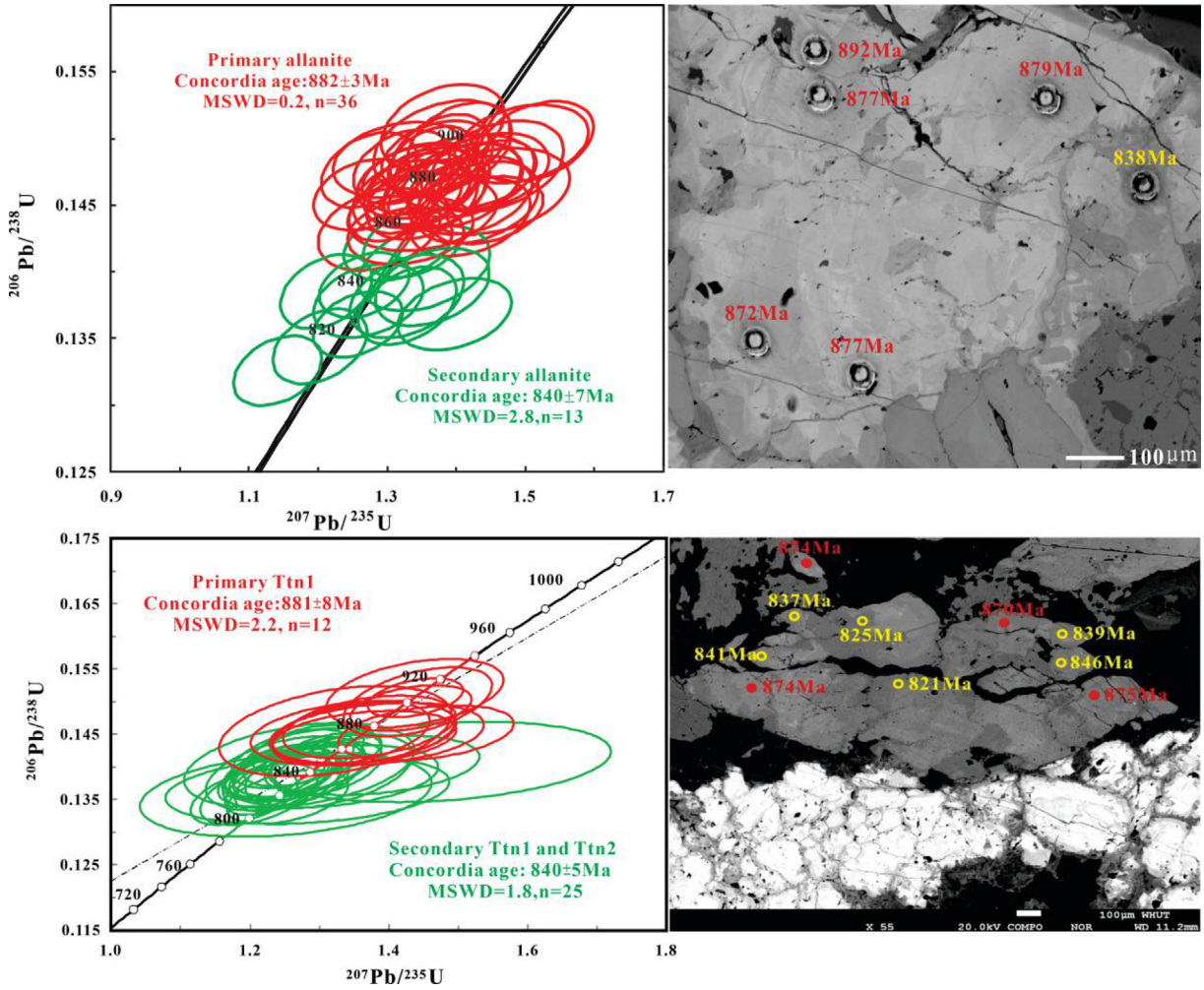

Fig. 11. Concordia diagram of U-Pb dating results for hydrothermal allanite (a) and titanite (b). Also shows the BSE images of selected allanite and titanite grains, and ages of spot analyses.

5.3. Neodymium isotopes of titanite

In situ Nd isotopic data of two type of titanite are summarized in Table 7. Both Ttn1 and Tnt2 grains show restricted $(^{143}Nd/^{144}Nd)_i$ values of 0.5111–0.5112 (n = 12) and 0.5113–0.5115 (n = 12), respectively. Using an age of 880 Ma for Ttn1 and 840 Ma for Ttn2, the $\varepsilon_{Nd}(t)$ values were calculated to range from −7.00 to −5.43 and −4.31 to −1.97, respectively.

6. Discussion

6.1. Hydrothermal origin of allanite and titanite

Allanite grains investigated in this study consist of large, euhedral, and zoned crystals. The primary allanite are closely associated with amphibole, titanite (Ttn1), and epidote, whereas the secondary varieties are associated with magnetite and chalcopyrite (Fig. 6b– d; 7c). In addition, the primary allanite crystals typically contain two-phase aqueous or daughter mineral-bearing primary fluid inclusions (Fig. 12a, b), further documenting its precipitation from hydrothermal fluids. They have relatively low Th contents (47–387 ppm) and Th/U ratios (0.15–1.07), which are consistent with compositional features of hydrothermal allanite from the Rakkurijärvi and Nautanen IOCG deposits, Kiruna District, Sweden (Th = 5–574 ppm, Th/U ratios = 0.4–23.5; Smith et al., 2009) and the Beiminghe iron skarn deposit, North China (Th = 6–1078 ppm, Th/U ratios = 0.07–11.6; Deng et al., 2014), but significantly different from magmatic allanite (Th > 5 wt%, Th/U > 100; e.g. Gregory et al. (2007)). The textural and compositional data thus suggest the investigated allanite grains are of hydrothermal origin and precipitated from the REE-mineralizing fluids, rather than xenocrystals or inherited grains from the wall rocks.

Ttn1 grains are closely associated with primary allanite, amphibole, and epidote (Fig. 6b, c), whereas Ttn2 are fine-grained and intergrown with magnetite, biotite, and chalcopyrite (Fig. 6h). The mineral assemblages and textural relations indicate that both types of titanite are of hydrothermal origin. This view is confirmed by the presence of abundant aqueous and daughter mineral-bearing primary fluid inclusions in titanite (Fig. 12c, d). In general, hydrothermal titanite has lower Th/U ratios than magmatic titanite (Aleinikoff et al., 2002; Gao et al., 2012; Deng et al., 2015). Ttn1 and Ttn2 from Sin Quyen have extremely low Th/U values ranging from 0.001 to 0.008 and 0.089 to 1.783, respectively. These Th/U values are consistent with hydrothermal titanite from many skarn deposits elsewhere (e.g. Li et al. (2010), Deng et al. (2015), Fu et al. (2016), Hu et al. (2017), Duan and Li (2017)). In addition, the titanite grains have relatively low REE contents and are characterized by relatively flat REE patterns with low LREE/HREE ratios of 0.60–4.04 (Table 4). The REEs feature contradicts to magmatic titanite that typically has much higher LREE/HREE ratios (Gao et al., 2012; Smith et al., 2009). The relatively depletion of LREE in Tnt1 can be interpreted as a result of co-precipitation of LREE enriched allanite (Fig. 6b, 7b).

Table 6
In situ LA-ICP-MS U–Th–Pb ages of the type 1 titanite and type 2 titanite in the Sin Quyen deposit.

Spots	$_{Common}$Pb ppm	$_{total}$Pb ppm	Th ppm	U ppm	Th/U	$^{207}Pb/^{206}Pb$		$^{207}Pb/^{206}Pb$		$^{207}Pb/^{235}U$	
						Ratio	2σ	Ratio	2σ	Ratio	2σ
Ttn1-01P	0.00	19.04	0.21	151	0.001	0.0677	0.0052	1.3456	0.0927	0.1451	0.0040
Ttn1-02S	0.00	18.10	0.42	149	0.003	0.0686	0.0043	1.3142	0.0798	0.1393	0.0037
Ttn1-03S	0.00	18.07	0.31	149	0.002	0.0690	0.0052	1.3174	0.1012	0.1386	0.0031
Ttn1-04P	0.00	17.24	0.60	135	0.004	0.0728	0.0052	1.4540	0.1033	0.1452	0.0034
Ttn1-05S	0.00	7.70	0.20	63	0.003	0.0687	0.0074	1.2828	0.1350	0.1365	0.0034
Ttn1-06P	0.00	13.85	0.80	104	0.008	0.0698	0.0055	1.4383	0.1041	0.1512	0.0043
Ttn1-07S	0.22	17.61	1.11	146	0.008	0.0671	0.0079	1.2514	0.1389	0.1358	0.0043
Ttn1-08P	1.99	12.66	0.28	98	0.003	0.0685	0.0054	1.3658	0.1080	0.1445	0.0033
Ttn1-09S	1.22	19.82	0.49	162	0.003	0.0657	0.0044	1.2517	0.0760	0.1390	0.0037
Ttn1-10S	1.47	15.95	0.33	128	0.003	0.0662	0.0061	1.2710	0.1095	0.1402	0.0043
Ttn1-11P	2.07	17.43	0.39	135	0.003	0.0662	0.0071	1.3232	0.1367	0.1455	0.0056
Ttn1-12P	1.66	16.03	0.34	123	0.003	0.0676	0.0064	1.3494	0.1211	0.1452	0.0040
Ttn1-13P	0.54	12.80	0.17	99	0.002	0.0691	0.0061	1.3831	0.1263	0.1450	0.0039
Ttn1-14P	1.91	20.99	0.34	156	0.002	0.0649	0.0064	1.4420	0.0875	0.1499	0.0043
Ttn1-15S	1.83	13.54	0.66	106	0.006	0.0766	0.0090	1.4751	0.1617	0.1408	0.0041
Ttn1-16S	0.26	23.63	0.25	189	0.001	0.0711	0.0051	1.3785	0.1005	0.1403	0.0030
Ttn1-17P	0.00	29.27	0.57	224	0.003	0.0696	0.0035	1.4323	0.0715	0.1490	0.0029
Ttn1-18P	2.75	54.88	1.50	410	0.004	0.0691	0.0027	1.4386	0.0564	0.1505	0.0024
Ttn1-19P	1.32	17.34	0.39	135	0.003	0.0679	0.0050	1.3723	0.1014	0.1461	0.0039
Ttn1-20P	0.76	14.68	0.45	116	0.004	0.0681	0.0052	1.3640	0.1074	0.1452	0.0039
Ttn2-01	0.58	72.96	139	556	0.250	0.0650	0.0027	1.2469	0.0508	0.1389	0.0027
Ttn2-02	0.70	58.74	132	430	0.308	0.0670	0.0027	1.3051	0.0556	0.1408	0.0029
Ttn2-03	0.13	61.52	160	441	0.362	0.0650	0.0029	1.2429	0.0541	0.1385	0.0030
Ttn2-04	1.13	44.39	177	292	0.607	0.0659	0.0031	1.2954	0.0622	0.1423	0.0024
Ttn2-05	0.00	53.79	194	379	0.513	0.0646	0.0029	1.2615	0.0585	0.1413	0.0030
Ttn2-06	0.19	40.30	183	262	0.699	0.0654	0.0030	1.2762	0.0578	0.1417	0.0031
Ttn2-07	1.63	76.18	173	563	0.308	0.0661	0.0024	1.2554	0.0511	0.1376	0.0029
Ttn2-08	0.13	41.97	69	313	0.219	0.0660	0.0032	1.2702	0.0632	0.1396	0.0028
Ttn2-09	0.00	59.93	43	475	0.089	0.0655	0.0026	1.2387	0.0491	0.1374	0.0031
Ttn2-10	2.32	40.46	67	307	0.220	0.0656	0.0032	1.2480	0.0623	0.1379	0.0027
Ttn2-11	0.40	60.18	109	450	0.242	0.0643	0.0024	1.2360	0.0501	0.1392	0.0028
Ttn2-12	0.43	62.89	111	477	0.232	0.0637	0.0025	1.1914	0.0508	0.1354	0.0028
Ttn2-13	0.73	44.88	175	321	0.544	0.0673	0.0033	1.2537	0.0577	0.1354	0.0027
Ttn2-14	0.60	56.94	246	392	0.628	0.0682	0.0026	1.3128	0.0511	0.1397	0.0027
Ttn2-15	0.36	52.43	211	371	0.568	0.0648	0.0026	1.2414	0.0507	0.1388	0.0023
Ttn2-16	1.82	53.69	156	401	0.389	0.0658	0.0028	1.2610	0.0562	0.1390	0.0028
Ttn2-17	1.57	65.64	123	525	0.235	0.0648	0.0030	1.2127	0.0558	0.1358	0.0031

Spots	$^{207}Pb/^{206}Pb$		$^{207}Pb/^{235}U$		$^{206}Pb/^{238}U$	
	Age (Ma)	2σ	Age (Ma)	2σ	Age (Ma)	2σ
Ttn1-01P	859	155	866	40	874	22
Ttn1-02S	887	130	852	35	841	21
Ttn1-03S	898	156	853	44	837	18
Ttn1-04P	1009	146	912	43	874	19
Ttn1-05S	900	224	838	60	825	20
Ttn1-06P	920	163	905	43	908	24
Ttn1-07S	839	281	824	63	821	24
Ttn1-08P	885	159	874	46	870	18
Ttn1-09S	796	140	824	34	839	21
Ttn1-10S	813	194	833	49	846	24
Ttn1-11P	813	224	856	60	875	32
Ttn1-12P	857	196	867	52	874	23
Ttn1-13P	902	184	882	54	873	22
Ttn1-14P	770	209	907	36	901	24
Ttn1-15S	1110	238	920	66	849	23
Ttn1-16S	959	146	880	43	846	17
Ttn1-17P	917	106	903	30	895	16
Ttn1-18P	902	84	905	24	904	14
Ttn1-19P	866	154	877	43	879	22
Ttn1-20P	872	166	874	46	874	22
Ttn2-01	776	87	822	23	838	15
Ttn2-02	839	85	848	25	849	16
Ttn2-03	776	93	820	25	836	17
Ttn2-04	1200	100	844	28	858	14
Ttn2-05	761	94	829	26	852	17
Ttn2-06	787	96	835	26	854	17
Ttn2-07	809	77	826	23	831	16
Ttn2-08	806	101	832	28	842	16
Ttn2-09	791	83	818	22	830	18
Ttn2-10	794	104	822	28	833	15

(*continued on next page*)

Table 6 (*continued*)

Spots	$^{207}Pb/^{206}Pb$		$^{207}Pb/^{235}U$		$^{206}Pb/^{238}U$	
	Age (Ma)	2σ	Age (Ma)	2σ	Age (Ma)	2σ
Ttn2-11	752	78	817	23	840	16
Ttn2-12	733	79	797	24	818	16
Ttn2-13	850	102	825	26	819	15
Ttn2-14	872	80	851	22	843	15
Ttn2-15	769	85	820	23	838	13
Ttn2-16	800	91	828	25	839	16
Ttn2-17	769	66	806	26	821	18

Note: P: primary, S: secondary.

Table 7
Sm-Nd isotopic data determined by LA-MC-ICP-MS for titanite from REE only and REE-Fe-Cu mineralization zone in the Sin Quyen deposit.

No	Sample	Age (Ma)	$^{147}Sm/^{144}Nd$	$^{143}Nd/^{144}Nd$	$(^{143}Nd/^{144}Nd)$ i	ε_{Nd} (t)
1	H474	880	0.2255	0.5125	0.5112	−5.80
2	H474	880	0.2177	0.5124	0.5112	−6.14
3	H474	880	0.2192	0.5124	0.5112	−6.22
4	H474	880	0.2302	0.5125	0.5112	−6.42
5	H474	880	0.2322	0.5125	0.5112	−5.85
6	H474	880	0.2155	0.5125	0.5112	−5.43
7	H474	880	0.2060	0.5124	0.5112	−5.81
8	H474	880	0.1917	0.5123	0.5112	−6.03
9	H474	880	0.2271	0.5125	0.5112	−6.18
10	H474	880	0.2637	0.5127	0.5111	−7.00
11	H474	880	0.1970	0.5123	0.5112	−6.57
12	H474	880	0.2221	0.5125	0.5112	−6.03
13	H505	840	0.0852	0.5119	0.5114	−3.02
14	H505	840	0.0762	0.5118	0.5114	−2.94
15	H505	840	0.1148	0.5120	0.5114	−3.31
16	H505	840	0.0782	0.5119	0.5115	−1.97
17	H505	840	0.0865	0.5118	0.5114	−3.76
18	H505	840	0.1009	0.5119	0.5114	−3.26
19	H505	840	0.1100	0.5120	0.5114	−2.48
20	H505	840	0.1029	0.5120	0.5114	−2.16
21	H505	840	0.0837	0.5118	0.5114	−3.60
22	H505	840	0.1218	0.5120	0.5113	−4.31
23	H505	840	0.0949	0.5119	0.5114	−3.68
24	H505	840	0.0703	0.5117	0.5113	−4.03

6.2. Reliability of the allanite and titanite U-Pb dates

In this study, both allanite and titanite yielded two ages at ~880 Ma and ~840 Ma, respectively. Therefore, it is necessary to evaluate the reliabilities of the U-Pb dating data. Previous studies have shown demonstrated that allanite can potentially contain high common Pb (> 90% Pb_{total}) and hence yield older U-Pb ages (Poitrasson, 2002; Kim et al., 2009, Darling et al., 2012). However, our results presented in this work have shown that hydrothermal allanite from the Sin Quyen IOCG Deposit contains essentially negligible common Pb, most of which are below the LA-ICPMS detection limit (Table 5). Thus, no common Pb corrections are need for the U-Pb ages of the studied allanite. This interpretation is also confirmed by the fact that most of the spot analyses yield concordant $^{206}Pb/^{238}U$ and $^{207}Pb/^{235}U$ ages (Table 5; Fig. 11a).

In the Sin Quyen deposit, both Ttn1 and Ttn2 contain high U and extremely low common Pb (Table 6). The very low common Pb contents indicate that common Pb corrections had no effects on the titanite U-Pb dates, as demonstrated by the concordant U-Pb ages of the Ttn1 and Ttn2 that formed two coherent groups on the U-Pb concordia diagrams (Fig. 10b). It is noted that the intergrown titanite and allanite yielded indistinguishable weighted mean $^{206}Pb/^{238}U$ ages (Fig. 11a, b), providing additional evidence for the reliability of titanite and allanite U-Pb ages. Therefore, we suggest that both ages obtained by allanite and titanite can represent their crystallization ages.

6.3. Timing and history of ore mineralization at Sin Quyen

Our new allanite and titanite U-Pb ages reveal two hydrothermal events in the Sin Quyen deposit at ca. 880 Ma and ca. 840 Ma, respectively. The primary allanite and Ttn1 have indistinguishable U-Pb ages of 882 ± 3 Ma and 881 ± 8 Ma, respectively, which are interpreted as the age of the early, REE-only mineralization of episode 1. The secondary allanite and Ttn2 have consistent U-Pb ages of 840 ± 7 Ma and 838 ± 5 Ma, respectively. These ages are reproducible within analytical uncertainties and consistent with U-Pb ages of hydrothermal zircon and monazite (841 ± 12 Ma and 836 ± 18 Ma) reported by Li et al. (2017). The secondary allanite and Ttn2 are associated with magnetite, chalcopyrite, and biotite of the episode 2 mineralization (Figs. 5 and 6), which are typical of mineral assemblages observed in many IOCG deposits worldwide. Therefore, in situ U-Pb ages of secondary allanite and Ttn2 represent the IOCG mineralization event of episode 2. Collectively, the allanite and titanite U-Pb ages presented here, together with previously zircon and monazite U-Pb data (Li et al., 2017b), substantiate two episodes of hydrothermal mineralization events at the Sin Quyen deposit (Fig. 13a). The different Nd isotopes of ~880 Ma and ~840 Ma titanite also provide convincing evidences that they were derived from different hydrothermal fluids.

Northern Vietnam was considered to be a part of the Yangtze Block by previous studies (Chung et al., 1998; Hieu et al., 2011; Li et al., 2017a). The two mineralization episodes of REE recognized in this study are roughly consistent with extensive Neoproterozoic magmatism, which has ages from ~880 Ma to ~760 Ma, in western Yangtze Block and northern Vietnam. Although Neoproterozoic (~880 to ~840 Ma) intrusions have not been observed in the mining district, slightly younger granitic intrusions (< 820 Ma) have been reported in the region (Hieu et al., 2009; Li et al., 2017a). It is possible that unexposed Neoproterozoic intrusions may be present beneath the Sin Quyen deposit, just as many IOCG deposits worldwide that do not show spatial association with igneous intrusions.

6.4. Metal sources of two episodes of mineralization

The utility of Nd isotopes as tracers of REE rich IOCG systems has been previously demonstrated (Johnson and McCulloch, 1995; Skirrow et al., 2007; Li et al., 2018). Titanite of the episode 1 mineralization have $\varepsilon_{Nd}(t)$ values ranging from −7.00 to −5.43, whereas titanite of the episode 2 have $\varepsilon_{Nd}(t)$ values of −4.31 to −1.97 (Table 7). The difference in Nd isotopic compositions between the two titanite generations is hence attributed to hydrothermal fluids of different sources. In addition, Nd isotopes of episode 1 titanite partly overlap those of the *meta*-sedimentary basement rocks (Li et al., 2017a; Fig. 14), likely reflecting interaction between magmatic fluids and the hosting rocks. Titanite of episode 2 mineralization has $\varepsilon_{Nd}(t)$ values similar to those of some felsic intrusions in the region (Fig. 14). This indicates that the REEs of the episode 2 mineralization and, by inference, the IOCG orebodies themselves, had a dominant source of magmatic fluids. However, exposed Neoproterozoic intrusions in the Ailao Shan Phan Si Pan

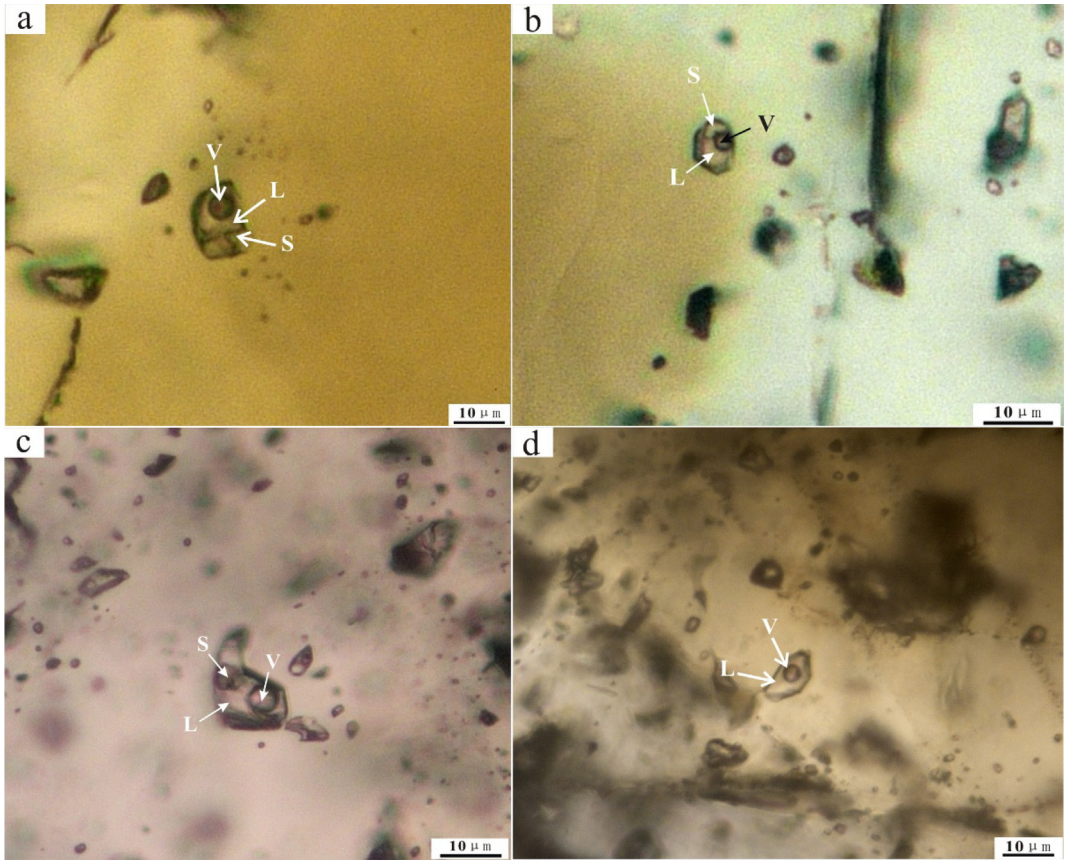

Fig. 12. (a, b) Photomicrographs showing primary fluid inclusions typically observed in allanite grains. (c, d) Photomicrographs showing primary fluid inclusions typically observed in titanite grain. L: liquid, V: vapor, S: sylvite.

belt are mostly younger than the Sin Quyen deposit, precluding the possibility that these granitoid rocks are the direct source of REE ores. It is more likely that REEs were derived from juvenile source, maybe mantle-derived magmas, beneath the deposit.

REE-bearing minerals in hydrothermal deposits are susceptible to fluid metasomatism during subsequent hydrothermal overprint, as marked by dissolution of old generations and re-precipitation of younger generations of various REE minerals (e.g. Smith et al. (2000), Harlov et al. (2005), Chen and Zhou (2015), Ismail et al. (2014), Kontonikas-Charos et al. (2014)). The Sin Quyen IOCG deposit is LREE-enriched, with allanite being the predominant REE mineral. Petrographic data (Figs. 6c, d, 7a, 11a) demonstrate that the primary allanite has been partly altered by later hydrothermal fluids to form the secondary allanite, forming the core-rim textures. Results of LA-ICP-MS analysis and X-ray mapping demonstrate that primary allanite contain LREE higher than the secondary variety (Fig. 8f–h and Tables 1, 2). This observation indicates that REEs were partially leached out during late stage hydrothermal event. Mineralogical associations show that Ttn2 grains are intergrown with magnetite and chalcopyrite (Fig. 6h), indicating their formation in the Fe-Cu mineralization stage of episode 2. However, LA-ICP-MS and EMP analyses of two types of titanite demonstrate that Ttn2 grains contain LREE that are one order of magnitude higher than the Ttn1 (Table 4; Fig. 10d). In situ Nd isotopes of Ttn2 have more depleted Nd isotopes, implying that it was precipitated from the episode 2 hydrothermal fluid. Ttn2 formed in the Fe-Cu mineralization stage is locally associated with the altered allanite (Fig. 7d). This observation suggests that such fluids were also responsible for the fluid metasomatism of primary allanite and Ttn1, and LREE leached from the allanite were also likely incorporated into newly formed LREE-bearing phases (Fig. 15b).

6.5. Comparison to the Kangdian IOCG metallogenic belt

The Sin Quyen deposits in northwestern Vietnam have a common paragenetic sequence of pre-ore sodic alteration, followed by magnetite-LREE mineralization and Cu-sulfide mineralization that are associated with Ca-Fe and potassic alteration, respectively. Such mineralization and alteration features are well comparable to the IOCG deposits in Kangdian belt, such as Lala, Yinachang, and Dahongshan deposits (e.g., Zhao and Zhou, 2011; Chen and Zhou, 2012; Zhou et al., 2014; Li and Zhou, 2015; Zhao et al., 2017). Thus, the Sin Quyen deposit was previously considered to be part of the Kangdian Fe-Cu province along the western Yangtze block (Fig. 1; Zhao and Zhou, 2011; Zhou et al., 2014). However, recent geochronological data have shown that the ore-hosting strata and ages of Cu-Fe mineralization in northwestern Vietnam and Kangdian belt are different. IOCG deposits in the Kangdian province are hosted within ~1.7 Ga strata, including the Dahongshan, Hekou, and Dongchuan groups, which are unconformably overlain by 1.1–1.0 Ga Kunyang and Huili groups (Zhao and Zhou, 2011; Chen and Zhou, 2012; Zhou et al., 2014; Li and Zhou, 2015). It should be noted that the 1.1–1.0 Ga strata widespread in the Kangdian belt do not host any IOCG deposits. The IOCG mineralization over the Kangdian belt occurred mainly at ~1.66 Ga, and was hydrothermally overprinted at 1.03 and 0.83 Ga as marked by numerous Cu-sulfide veins (Zhao et al., 2017; 2019). These veins are considered to reflect post-ore remobilization rather than an independent IOCG mineralization event (Zhao et al., 2017). However, the mineralization ages of 880 Ma and 840 Ma identified at Sin Quyen are significantly younger than IOCG deposits in the Kangdian belt. More importantly, recent studies have shown that the Sin Quyen and the equivalent Longbohe group along the ASRR should be dismembered into the ~1.7 Ga Lower group and ~ 0.9 Ga Upper group (Li et al., 2017a; Liu and Chen, 2019).

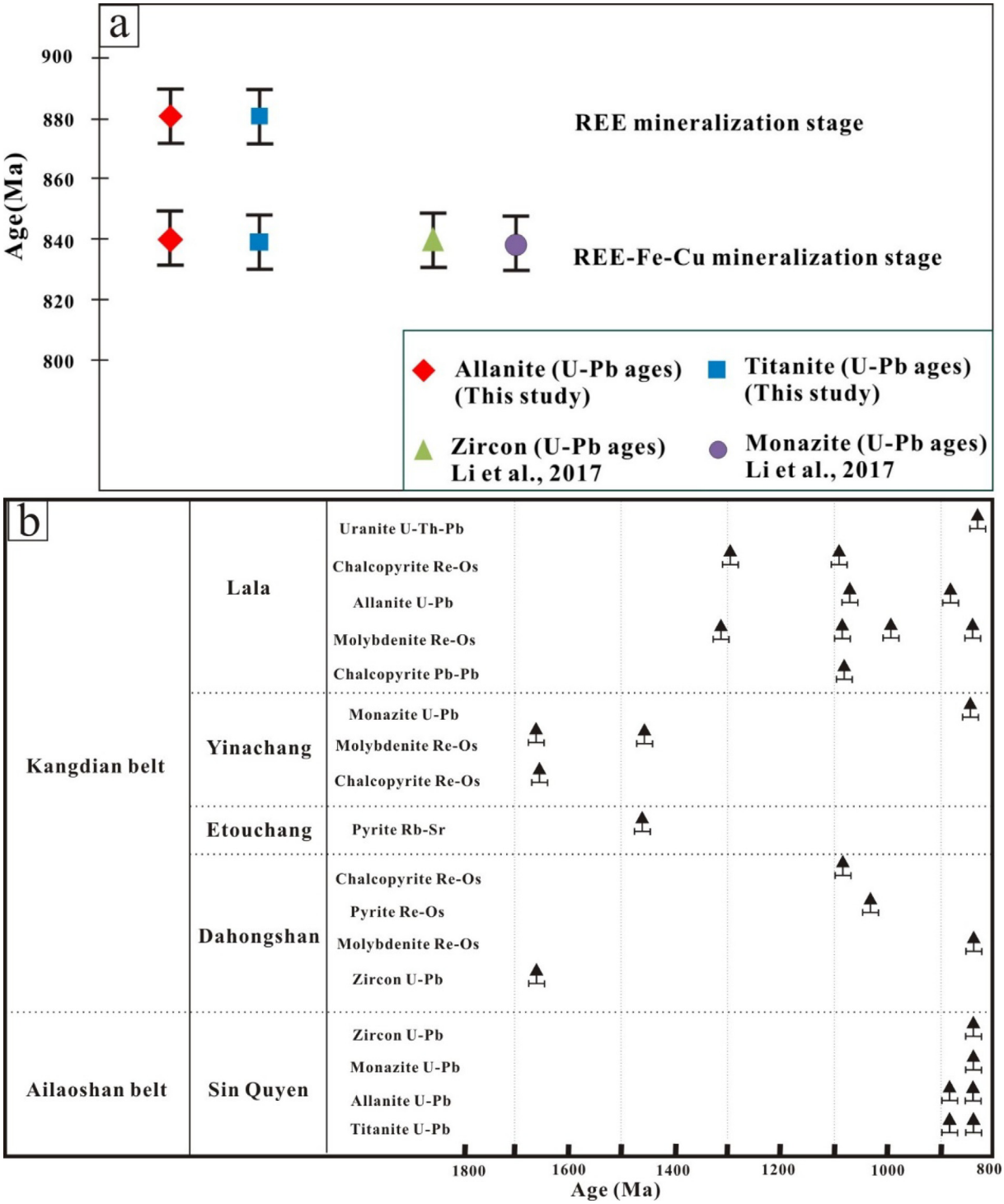

Fig. 13. (a) Summary of geochronological data for the Sin Quyen deposit. (b) Summary of geochronological data showing the timing of mineralization events for the Kangdian Copper Belt and Sin Quyen deposit (after Zhu et al. (2017)).

Both Sin Quyen and Longbohe deposits are hosted in the 0.9 Ga Upper group, and were hence formed in different tectonic setting compared to those in the Kangdian belt. Neoproterozoic magmatic rocks are well-developed at Sin Quyen and surrounding areas, which were emplaced at 824–723 Ma (Hieu et al., 2009; Wang et al., 2011; Li et al., 2017a) and are generally considered to be formed in a subduction related continental setting (Zhou et al., 2002, 2006; Hieu et al., 2009; Li et al., 2017a).

The above-statements led us to suggest that the northwestern Vietnam may not have a ~1.66 Ga IOCG mineralization event as recognized in the Kangdian belt along the western Yangtze block. The relatively young mineralization event of 880–840 Ma in the Sin Quyen deposit suggest that IOCG deposits along the ASRR likely formed in a back-arc tectonic setting of Neoproterozioc subduction, similar to the scenario of the Mesozoic IOCG deposits in Central Andes. This finding has implications for future exploration for IOCG deposits in north-western Vietnam.

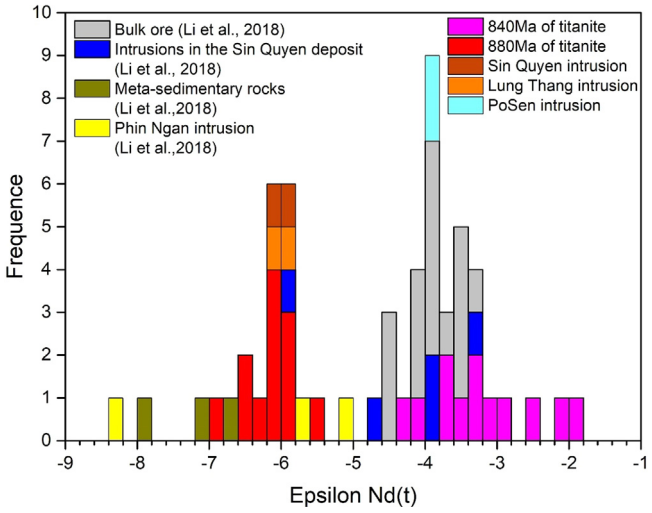

Fig. 14. Histograms showing variations of $\varepsilon_{Nd}(t)$ for titanite (this study), Neoproterozoic crust-derived felsic intrusions, and ore hosting metasedimentary rocks. The Neoproterozoic crust-derived felsic intrusions include the Phin Ngan pluton (824 Ma) (Li et al., 2017a), Posen pluton (750 Ma) (Lan et al., 2001), granitic dikes/stocks from the Sin Quyen mine (758–736 Ma) (Li et al., 2017a, this study) and Lung Thang pluton (800 Ma) (this study).

7. Conclusions

Two episodes of alteration and mineralization have been identified in the Sin Quyen deposit. Episode 1 is dominated by intense Ca alteration and associated REE-only mineralization. Episode 2 includes pre-ore Na alteration, *syn*-ore Ca-Fe and K-Fe alteration with associated IOCG mineralization. New allanite and titanite U-Pb dating results provide precise constraints on the timing and evolution of REE and Fe-Cu-Au mineralization at ~880 Ma and ~840 Ma, respectively. Episode 1 titanite have $\varepsilon_{Nd}(t)$ values ranging from −7.00 to −5.43, which are lower than episode 2 titanite of the main stage IOCG mineralization having $\varepsilon_{Nd}(t)$ values from −4.31 to −1.97. These values are similar to those of the Neoproterozoic intrusions, indicating a possible magmatic source for the REEs mineralization. These results place important constraints on onset timing of IOCG mineralization along the Ailao Shan belt, which was considered to be part of metallogenic belt in Southwest China. IOCG deposits along the Ailao Shan belt were likely formed in a back-arc extensional setting during Neoproterozoic subduction.

Declaration of Competing Interest

The authors declare that they have no known competing financial interests or personal relationships that could have appeared to influence the work reported in this paper.

Acknowledgements

This study was supported by the NSFC Projects (41822203, 41972074 and 41472068) and the Fundamental Research Funds for the Central Universities (CUG140618). We would like to express our thanks to Dr. Do Van Nhuan from Hanoi University of miming and Geology and Pham Quoc Duy, Do Van Hung of Sin Quyen Company for their help in the fieldwork and data collection. Great thanks are extended to Zhuang Duan, Wen-Sheng Gao, Hong-Qiang Wang, and Run-Jie Zhou for their help with LA-ICPMS, EPMA, and SEM analyses. This is contribution 27 of CREGET (Center for Research in Economic Geology and Exploration Targeting).

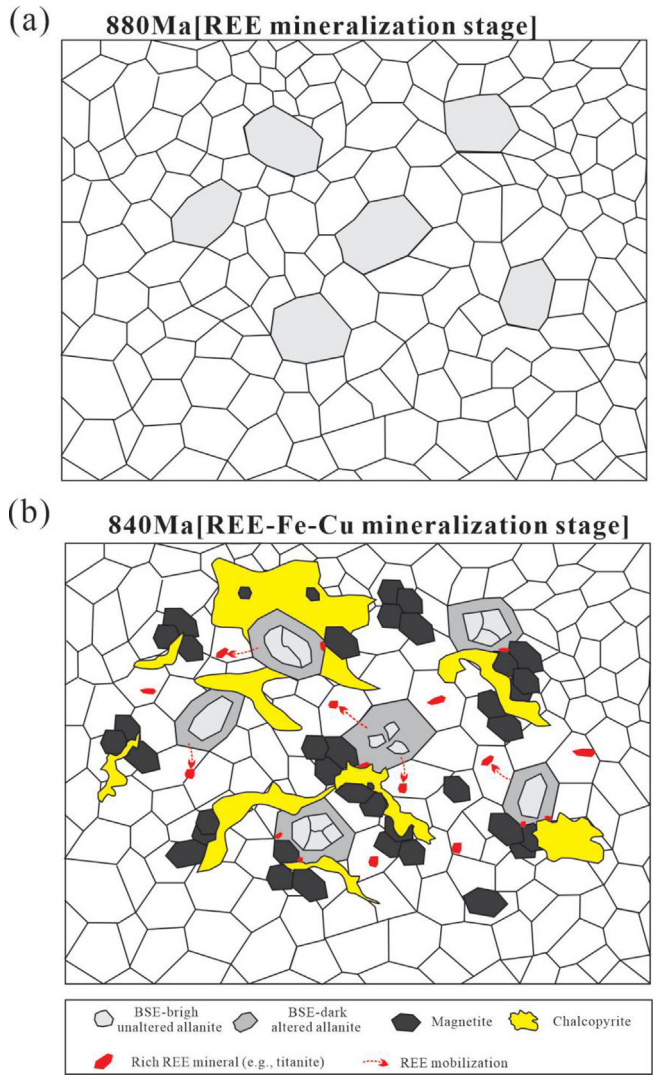

Fig. 15. Cartoons illustrating the REE mineralization and remobilization histories of the Sin Quyen deposit. (a) In the first mineralization stage, only REE-rich allanite were formed; (b) In the second mineralization stage, it was the main ore-forming stage of IOCG ores. The second stage hydrothermal fluid also altered the primary allanite.

Appendix A. Supplementary data

Supplementary data to this article can be found online at https://doi.org/10.1016/j.oregeorev.2020.103676.

References

Aleinikoff, J.N., Wintsch, R.P., Fanning, C.M., Dorais, M.J., 2002. U-Pb geochronology of zircon and polygenetic titanite from the Glastonbury Complex, Connecticut, USA: an integrated SEM, EMPA, TIMS, and SHRIMP study. Chem. Geol. 188 (1), 125–147.
Barton, M.D., 2014. Iron Oxide(Cu-Au-REE-P-Ag-U-Co) Systems. Treatise Geochem. 515–541.
Cai, Y.F., Wang, Y.J., Cawood, P.A., Fan, W.M., Liu, H.C., Xing, X.W., Zhang, Y.Z., 2014. Neoproterozoic subduction along the Ailaoshan zone, South China: Geochronological and geochemical evidence from amphibolite. Precambr. Res. 245, 13–28.
Cai, Y.F., Wang, Y.J., Cawood, P.A., Zhang, Y.Z., Zhang, A.M., 2015. Neoproterozoic crustal growth of the Southern Yangtze Block: Geochemical and zircon U-Pb geochronological and Lu-Hf isotopic evidence of Neoproterozoic diorite from the Ailaoshan zone. Precambr. Res. 266, 137–149.
Cao, M.J., Qin, K.Z., Li, G.M., Evans, N.J., Jin, L.Y., 2015. In situ LA-(MC)-ICP-MS trace element and Nd isotopic compositions and genesis of polygenetic titanite from the Baogutu reduced porphyry Cu deposit, Western Junggar, NW China. Ore Geol. Rev. 65, 940–954.
Casquet, C., Galindo, C., Tornos, F., Velasco, F., Canales, A., 2001. The Aguablanca Cu–Ni ore deposit (Extremadura, Spain), a case of synorogenic orthomagmatic

mineralization: age and isotope composition of magmas (Sr, Nd) and ore (S). Ore Geol. Rev. 18 (3), 237–250.
Chen, W.T., Zhou, M.F., 2012. Paragenesis, stable isotopes, and molybdenite Re-Os isotope age of the Lala Iron-Copper deposit, Southwest China. Econ. Geol. 107 (3), 459–480.
Chen, W.T., Zhou, M.F., 2014. Ages and compositions of primary and secondary allanite from the Lala Fe–Cu deposit, SW China: implications for multiple episodes of hydrothermal events. Contrib. Miner. Petrol. 168 (2).
Chen, W.T., Zhou, M.F., 2015. Mineralogical and geochemical constraints on mobilization and mineralization of rare Earth elements in the Lala Fe-Cu-(Mo, REE) deposit, SW China. Am. J. Sci. 315 (7), 671–711.
Chung, S.L., Lo, C.H., Lee, T.Y., Zhang, Y.Q., 1998. Diachronous uplift of the Tibetian plateau starting 40 Myr ago. Nature 394 (6695), 769.
Darling, J.R., Storey, C.D., Engi, M., 2012. Allanite U-Th-Pb geochronology by laser ablation ICPMS. Chem. Geol. 292–293, 103–115.
Deng, X.D., Li, J.W., Wen, G., 2014. Dating iron skarn mineralization using hydrothermal allanite-(La) U-Th–Pb isotopes by laser ablation ICP-MS. Chem. Geol. 382, 95–110.
Deng, X.D., Li, J.W., Zhou, M.F., Zhao, X.F., Yan, D.R., 2015. In-situ LA-ICPMS trace elements and U-Pb analysis of titanite from the Mesozoic Ruanjiawan W–Cu–Mo skarn deposit, Daye district, China. Ore Geol. Rev. 65, 990–1004.
Duan, Z., Li, J.W., 2017. Zircon and titanite U-Pb dating of the Zhangjiawa iron skarn deposit, Luxi district, North China Craton: Implications for a craton-wide iron skarn mineralization. Ore Geol. Rev. 89, 309–323.
Fu, Y., Sun, X.M., Zhou, H.Y., Lin, H., Yang, T.J., 2016. In-situ LA–ICP–MS U-Pb geochronology and trace elements analysis of polygenetic titanite from the giant Beiya gold–polymetallic deposit in Yunnan Province, Southwest China. Ore Geol. Rev. 77, 43–56.
Gao, X.Y., Zheng, Y.F., Chen, Y.X., Guo, J.L., 2012. Geochemical and U-Pb age constraints on the occurrence of polygenetic titanites in UHP metagranite in the Dabie orogen. Lithos 136–139, 93–108.
Giere, R., Sorensen, S.S., 2004. Allanite and other REE-rich epidote-group minerals. Rev. Mineral. Geochem. 56 (1), 431–493.
Gregory, C.J., Rubatto, D., Allen, C.M., Williams, I.S., Hermann, J., Ireland, T., 2007. Allanite micro-geochronology: a LA-ICP-MS and SHRIMP U-Th-Pb study. Chem. Geol. 245 (3–4), 162–182.
Groves, D.I., Bierlein, F.P., Meinert, L.D., Hitzman, M.W., 2010. Iron oxide copper-gold (IOCG) deposits through Earth history: implications for origin, lithospheric setting, and distinction from other epigenetic iron oxide deposits. Econ. Geol. 105 (3), 641–654.
Harlov, D.E., Wirth, R., Förster, H.J., 2005. An experimental study of dissolution–reprecipitation in fluorapatite: fluid infiltration and the formation of monazite. Contrib. Miner. Petrol. 150 (3), 268–286.
Hieu, P.T., Nguyen, T.B.T., Bui, M.T., Nguyen, Q.L., Chen, F.K., Zhu, X.Y., Wang, W., 2009. Zircon U-Pb ages and Hf isotopic composition of the Posen granite in northwestern Vietnam. Acta Petrol. Sin. 25 (12), 3141–3152.
Hieu, P.T., Chen, F., Me, L.T., Thuy, N.T.B., Siebel, W., Lan, T.G., 2011. Zircon U-Pb ages and Hf isotopic compositions from the Sin Quyen Formation: the Precambrian crustal evolution of northwest Vietnam. Int. Geol. Rev. 54 (13), 1548–1561.
Hieu, P.T., Chen, F.K., Thuy, N.T.B., Cuong, N.Q., Li, S.Q., 2013. Geochemistry and zircon U-Pb ages and Hf isotopic composition of Permian alkali granitoids of the Phan Si Pan zone in northwestern Vietnam. J. Geodyn. 69, 106–121.
Hieu, P.T., Chen, F.K., Zhu, X.Y., Wang, F., 2010. Zircon ages of paragneisses from the Sinh Quyen formation in Northwestern Vietnam and their geological significances. Earth Sci. J. China Univ. Geosci. 35 (2), 201–210 Diqiu Kexue – Zhongguo Dizhi Daxue Xuebao.
Hitzman, M.W., Oreskes, N., Einaudi, M.T., 1992. Geological characteristics and tectonic setting of proterozoic iron oxide (Cu-U-Au-REE) deposits. Precambr. Res. 58 (1), 241–287.
Hu, H., Li, J.W., Farlane, M.c., Christopher, R.M., Luo, Y., Mc Carron, T., 2017. Textures, trace element compositions, and U-Pb ages of titanite from the Mangling granitoid pluton, East Qinling Orogen: Implications for magma mixing and destruction of the North China Craton. Lithos 284–285, 50–68.
Hu, Z.C., Gao, S., Liu, Y.S., Hu, S.H., Chen, H.H., Yuan, H.L., 2008. Signal enhancement in laser ablation ICP-MS by addition of nitrogen in the central channel gas. J. Anal. At. Spectrom. 23 (8), 1093.
Hu, Z.C., Zhang, W., Liu, Y.S., Gao, S., Li, M., Zong, K.Q., Chen, H.H., Hu, S.H., 2015. "Wave" signal-smoothing and mercury-removing device for laser ablation quadrupole and multiple collector ICPMS analysis: application to lead isotope analysis. Anal Chem. 87 (2), 1152–1157.
Ishihara, S., Hirano, H., Hoshino, M., Pham, N.C., Pham, T.D., Tran, T.A., 2011. Mineralogical and chemical characteristics of the allanite-rich copper and iron ores from the Sin Quyen mine, northern Vietnam. Bull Geol Surv Jpn 62, 197–209.
Ismail, R., Ciobanu, C.L., Cook, N.J., Teale, G.S., Giles, D., Mumm, A.S., Wade, B., 2014. Rare earths and other trace elements in minerals from skarn assemblages, Hillside iron oxide–copper–gold deposit, Yorke Peninsula, South Australia. Lithos 184–187, 456–477.
Johnson, J.P., McCulloch, M.T., 1995. Sources of mineralizing fluids for the Olympic Dam deposit (South-Australia)-Sm-Nd Isotopic constraints. Chem. Geol. 121 (1–4), 177–199.
Kim, Y., Cheong, C.S., Lee, Y., Williams, I.S., 2009. SHRIMP allanite U-Th-Pb dating of bimodal Triassic metamorphism of Neoarchean tonalitic gneisses, Daeijak Island, central Korea. Geosci. J. 13 (3), 305–315.
Kontonikas-Charos, A., Ciobanu, C.L., Cook, N.J., 2014. Albitization and redistribution of REE and Y in IOCG systems: Insights from Moonta-Wallaroo, Yorke Peninsula, South Australia. Lithos 208–209, 178–201.
Lan, C.Y., Chung, S.L., Lo, C.H., Lee, T.Y., Wang, P.L., Li, H.M., Van Toan, D., 2001. First evidence for Archean continental crust in northern Vietnam and its implications for crustal and tectonic evolution in Southeast Asia. Geology 29 (3), 219–222.
Leloup, P.H., Lacassin, R., Tapponnier, P., Schärer, U., Zhong, D.L., Liu, X.H., Zhang, L.S., Ji, S.C., Trinh, P.T., 1995. The Ailao Shan-Red River shear zone (Yunnan, China), Tertiary transform boundary of Indochina. Tectonophysics 251 (1–4), 3–10.
Li, J.W., Deng, X.D., Zhou, M.F., Liu, Y.S., Zhao, X.F., Guo, J.L., 2010. Laser ablation ICP-MS titanite U-Th–Pb dating of hydrothermal ore deposits: a case study of the Tonglushan Cu-Fe-Au skarn deposit, SE Hubei Province, China. Chem. Geol. 270 (1–4), 56–67.
Li, X.C., Zhou, M.F., 2015. Multiple stages of hydrothermal REE remobilization recorded in fluorapatite in the Paleoproterozoic Yinachang Fe-Cu-(REE) deposit, Southwest China. Geochim. Cosmochim. Acta 166, 53–73.
Li, X.C., Zhao, J.H., Zhou, M.F., Gao, J.F., Sun, W.H., Tran, M.D., 2017a. Neoproterozoic granitoids from the Phan Si Pan belt, Northwest Vietnam: Implication for the tectonic linkage between Northwest Vietnam and the Yangtze Block. Precambr. Res. 309, 212–230.
Li, X.C., Zhou, M.F., 2018. The Nature and Origin of Hydrothermal REE Mineralization in the Sin Quyen Deposit, Northwestern Vietnam. Econ. Geol. 113 (3), 645–673.
Li, X.C., Zhou, M.F., Chen, W.T., Zhao, X.F., Tran, M.D., 2017b. Uranium-lead dating of hydrothermal zircon and monazite from the Sin Quyen Fe-Cu-REE-Au-(U) deposit, northwestern Vietnam. Miner. Deposita 53 (3), 399–416.
Li, X.C., Zhou, M.F., Yang, Y.H., Zhao, X.F., Gao, J.F., 2018. Disturbance of the Sm-Nd isotopic system by metasomatic alteration: a case study of fluorapatite from the Sin Quyen Cu-LREE-Au deposit, Vietnam. Am. Mineral. 103 (9), 1487–1496.
Liu, H.C., Wang, Y.J., Cawood, P.A., Fan, W.M., Cai, Y.F., Xing, X.W., 2015a. Record of Tethyan ocean closure and Indosinian collision along the Ailaoshan suture zone (SW China). Gondwana Res. 27 (3), 1292–1306.
Liu, L., Chen, T.W., 2019. Geology, mineralization styles and age of ore-hosting rocks of the Proterozoic Longbohe-Sin Quyen Fe-Cu belt: Implications for regional metallogeny. Ore Geol. Rev. 111.
Liu, J.L., Chen, X.Y., Wu, W.B., Tang, Y., Tran, M.D., Nguyen, Q.L., Zhang, Z.C., Zhao, Z.D., 2015b. New tectono-geochronological constraints on timing of shearing along the Ailao Shan-Red River shear zone: implications for genesis of Ailao Shan gold mineralization. J. Asian Earth Sci. 103, 70–86.
Liu, Y.S., Gao, S., Hu, Z.C., Gao, C.G., Zong, K.Q., Wang, D.B., 2010. Continental and oceanic crust recycling-induced melt-peridotite interactions in the trans-North China Orogen: U-Pb dating, Hf isotopes and trace elements in zircons from mantle xenoliths. J. Petrol. 51 (1–2), 537–571.
Ludwig, K.R., 2003. Isoplot 3.0: a geochronological toolkit for Microsoft Excel. Berkeley Geochronol. Center Special Publ. 4, 1–75.
Mclean, R.N., 2001. The Sin Quyen iron oxide-copper-gold-rare earth oxide mineralization of North Vietnam, In: Porter, T.M. (Ed.), Hydrothermal iron oxide copper–gold & related deposits: a global perspective, vol. 2. PGC Publishing, Adelaide, pp. 293–301.
Pham, Q.D., 2015. Exploration report on no.3 and no.7 orebodies of the Sin Quyen copper deposit, Lao Cai Province (in Vietnamese), pp. 1–85.
Petrik, I., Broska, I., Lipka, J., Siman, P., 1995. Granitoid allanite-(Ce): substitution relations, redox conditions and REE distributions (on an example of I-type granitoids, western Carpathians, Slovakia). Geol. Carpath. 46 (2), 79–94.
Poitrasson, F., 2002. In situ investigations of allanite hydrothermal alteration: examples from calc-alkaline and anorogenic granites of Corsica (southeast France). Contrib. Miner. Petrol. 142 (4), 485–500.
Qi, X.X., Zeng, L.S., Zhu, L.H., Hu, Z.C., Hou, K.J., 2012. Zircon U-Pb and LuHf isotopic systematics of the Daping plutonic rocks: implications for the Neoproterozoic tectonic evolution of the northeastern margin of the Indochina block, Southwest China. Gondwana research 21, 180–193.
Scherrer, N.C., Engi, M., Gnos, E., Jakob, V., Liechti, A., 2000. Monazite analysis, from sample preparation to microprobe age dating and REE quantification. Schweiz. Mineral. Petrogr. Mitt. 80 (1), 93–105.
Skirrow, R.G., Bastrakov, E.N., Barovich, K., Fraser, G.L., Creaser, R.A., Fanning, C.M., Raymond, O.L., Davidson, G.J., 2007. Timing of iron oxide Cu-Au-(U) hydrothermal activity and Nd isotope constraints on metal sources in the Gawler craton, South Australia. Econ. Geol. 102 (8), 1441–1470.
Smith, M.P., Henderson, P., Campbell, L.S., 2000. Fractionation of the REE during hydrothermal processes: constraints from the Bayan Obo Fe-REE-Nb deposit, Inner Mongolia, China. Geochim. Cosmochim. Acta 64 (18), 3141–3160.
Smith, M.P., Storey, C.D., Jeffries, T.E., Ryan, C., 2009. In situ U-Pb and trace element analysis of accessory minerals in the Kiruna District, Norrbotten, Sweden: new constraints on the timing and origin of mineralization. J. Petrol. 50 (11), 2063–2094.
Spandler, C., Hammerli, J., Sha, P., Hilbert-Wolf, H., Hu, Y., Roberts, E., Schmitz, M., 2016. MKED1: A new titanite standard for in situ analysis of Sm–Nd isotopes and U-Pb geochronology. Chem. Geol. 425, 110–126.
Ta, V.D., 1975. The Geological Report on Detailed Exploration of the Sin Quyen Copper Deposit (in Vietnamese). General Department of Geology and Minnerals of Vietnam, pp. 1–518.
Tapponnier, P., Tapponnier, P., Lacassin, R., Lacassin, R., Leloup, P.H., Leloup, P.H., Schärer, U., Schärer, U., Dalai, Z., Haiwei, W., Xiaohan, L., Shaocheng, J., Lianshang, Z., Jiayou, Z., 1990. The Ailao Shan/Red River metamorphic belt: tertiary left-lateral shear between Indochina and South China. Nature 343 (6257), 431–437.
Tran, M.D., Liu, J.L., Li, X.C., Dang, M.C., 2016. Geology, Fluid Inclusion and Isotopic Study of the Neoproterozoic Suoi Thau Copper Deposit, Northwest Vietnam. Acta Geol. Sin. 90 (3), 913–927.
Tran, T.H., Tran, T.A., Lan, C.Y., Usuki, T., Shellnutt, J.G., Pham, N.C., Pham, T.D., Ngo, T.P., Izokh, A.E., Borisenko, A.S., 2015. Petrogenesis of Late Permian silicic rocks of Tu Le basin and Phan Si Pan uplift (NW Vietnam) and their association with the Emeishan large igneous province. J. Asian Earth Sci. 109, 1–19.
Usuki, T., Lan, C.Y., Tran, T.H., Pham, T.D., Wang, K.L., Shellnutt, G.J., Chung, S.L., 2015.

Zircon U-Pb ages and Hf isotopic compositions of alkaline silicic magmatic rocks in the Phan Si Pan-Tu Le region, northern Vietnam: identification of a displaced western extension of the Emeishan Large Igneous Province. J. Asian Earth Sci. 97, 102–124.
Wang, P.L., Lo, C.H., Lan, C.Y., Chung, S.L., Lee, T.Y., Nam, T.N., Sano, Y., 2011. Thermochronology of the PoSen complex, northern Vietnam: Implications for tectonic evolution in SE Asia. J. Asian Earth Sci. 40 (5), 1044–1055.
Xiao, L., Zhang, H.F., Ni, P.Z., Xiang, H., Liu, X.M., 2007. LA-ICP-MS U-Pb zircon geochronology of early Neoproterozoic mafic-intermediat intrusions from NW margin of the Yangtze Block, South China: Implication for tectonic evolution. Precambr. Res. 154 (3–4), 221–235.
Xu, L., Hu, Z.C., Zhang, W., Yang, L., Liu, Y.S., Gao, S., Luo, T., Hu, S.H., 2015. In situ Nd isotope analyses in geological materials with signal enhancement and non-linear mass dependent fractionation reduction using laser ablation MC-ICP-MS. J. Anal. At. Spectrom. 30 (1), 232–244.
Zhao, X.F., Zhou, M.F., 2011. Fe-Cu deposits in the Kangdian region, SW China: a Proterozoic IOCG (iron-oxide-copper-gold) metallogenic province. Miner. Deposita 46 (7), 731–747.
Zhao, X.F., Zhou, M.F., Li, J.W., Wu, F.Y., 2008. Association of Neoproterozoic A- and I-type granites in South China: Implications for generation of A-type granites in a subduction-related environment. Chem. Geol. 257 (1), 1–15.
Zhao, X.F., Zhou, M.F., Su, Z.K., Li, X.C., Chen, W.T., Li, J.W., 2017. Geology, geochronology, and geochemistry of the Dahongshan Fe-Cu-(Au-Ag) deposit, Southwest China: Implications for the formation of iron oxide copper-gold deposits in intracratonic rift settings. Econ. Geol. 112 (3), 603–628.
Zhao, X.F., Chen, W.T., Li, X.C., Zhou, M.F., 2019. Iron Oxide Copper-Gold Deposits in China: A Review and Perspectives on Ore Genesis. In: Goldfarb, R., Chang, Z. (Eds.), Mineral Deposits of China. SEG Special Publication, pp. 553–580.
Zhou, M., Ma, Y., Yan, D., Xia, X., Zhao, J., Sun, M., 2006. The Yanbian Terrane (Southern Sichuan Province, SW China): a Neoproterozoic arc assemblage in the western margin of the Yangtze Block. Precambr. Res. 144 (1–2), 19–38.
Zhou, M.F., Yan, D.P., Kennedy, A.K., Li, Y., Ding, J., 2002. SHRIMP U-Pb zircon geochronological and geochemical evidence for Neoproterozoic arc-magmatism along the western margin of the Yangtze Block, South China. Earth Planet. Sci. Lett. 196 (1), 51–67.
Zhou, M.F., Zhao, X.F., Chen, W.T., Li, X.C., Wang, W., Yan, D.P., Qiu, H.N., 2014. Proterozoic Fe–Cu metallogeny and supercontinental cycles of the southwestern Yangtze Block, southern China and northern Vietnam. Earth Sci. Rev. 139, 59–82.
Zhu, Z.M., Tan, H.Q., Liu, Y.D., Li, C., 2017. Multiple episodes of mineralization revealed by Re-Os molybdenite geochronology in the Lala Fe-Cu deposit, SW China. Mineralium Deposita 53 (3), 311–322.